Journal of Environmental Chemical Engineering 10 (2022) 107612

Contents lists available at ScienceDirect

Journal of Environmental Chemical Engineering

journal homepage: www.elsevier.com/locate/jece

Ce-doped cobalt aluminate catalysts for the glycerol hydrodeoxygenation (HDO) with *in-situ* produced hydrogen

A.J. Reynoso [a], U. Iriarte-Velasco [b], M.A. Gutiérrez-Ortiz [a], J.L. Ayastuy [a,*]

[a] Department of Chemical Engineering, Faculty of Science and Technology, University of the Basque Country UPV/EHU, Sarriena S/N, 48940 Leioa, Spain
[b] Department of Chemical Engineering, Faculty of Pharmacy, University of the Basque Country UPV/EHU, Paseo de la Universidad, 7, 01006 Vitoria, Spain

ARTICLE INFO

Editor: Fumitake Takahash

Keywords:
Glycerol
Hydrodeoxygenation
In-situ hydrogen
1,2-Propanediol
Cobalt
Cerium

ABSTRACT

In this study, the hydrodeoxygenation (HDO) of glycerol with in-situ produced H_2, via aqueous-phase reforming, was investigated over Ce-doped $CoAl_2O_4$ catalysts synthesized by coprecipitation. The catalytic runs were performed at 50 bar/260 ºC for 3 h TOS in a fixed bed reactor. The synthesized catalysts were extensively characterized to better understand the effect of physicochemical and surface characteristics on the catalytic performance. The results revealed that doping with Ce increases the population and strength of acid centers, which results in a higher selectivity towards deoxygenated liquid products. Ce-doped catalysts exhibited higher yield to hydroxyacetone and 1,2-propanediol. Post-reaction characterization revealed a decrease of the metallic surface area, mainly due to alumina coating, and to a lesser extent, due to the oxidation and leaching of the cobalt.

1. Introduction

The need to diminish fossil fuel dependence in the chemical industry has led to the intensification of bio-based alternative products. Bio-based chemicals, products that are derived from biomass and other biological materials, are pivotal to the development of a more innovative and low-emissions economy while ensuring biodiversity and environmental protection [1]. The use of bio-based chemicals have raised as an alternative to standard chemicals since their environmental footprint is limited compared to their traditional counterparts. From a technical point of view, almost all the fuels and chemicals normally produced from fossil feedstocks can be produced from biomass in the so-called biorefinery [2]. Thus, bio-chemicals could drive a new economy model based on more thoughtful uses of natural resources. Hence, the European Commission aims to accelerate the market uptake of bio-chemicals, and estimates an annual growth rate of around 3.6% per year from 2018 to 2025, what represents an important expanding sector [1]. At present, researchers and entrepreneurs are involved in the development and commercialization not only of biofuels, but also of bio-derived replacements for basic chemicals. The path to a more sustainable industry will inevitably depend on the development of new high value-added chemicals, via catalytic process, from renewable sources [3].

A very attractive platform chemical from biomass is glycerol, which was identified as a top 12 bio-based chemical by the US Department of Energy [4]. Production of chemicals from raw glycerol is a good alternative to absorb the glycerol surplus generated from biodiesel industries. Several products can be obtained from glycerol, either gaseous products (i.e. hydrogen, syngas, alkanes, etc.), as well as high value-added liquid products (i.e. hydroxyacetone, pyruvaldehyde, acrolein, propanal, lactic acid, glyceric acid, acetaldehyde, etc.) [5–10].

Another valuable chemical that can be produced from hydrogenolysis of glycerol is 1,2-propanediol. It is widely used in the synthesis of unsaturated polyester resins, as coolant and also in pharmaceutical, food, and cosmetics formulations [11]. Currently, 1,2-propanediol is produced through the hydration of propylene oxide, which in turn comes from the selective oxidation of propylene, a fossil resource [12].

Conversion of glycerol to 1,2-propanediol involves the removal of an oxygen atom by the addition of hydrogen (C-O bond cleavage with simultaneous hydrogen addition), a catalytic reaction known as hydrodeoxygenation (HDO). The conventional way to carry out this process requires an external H_2 supply, usually derived from fossil fuels, which increases the cost and can generate safety issues due to the high diffusivity and flammability of molecular hydrogen [13]. In addition, hydrogen can block metal centers causing an inhibitory effect on catalytic activity [14]. Other explored alternative is the catalytic transfer

* Corresponding author.
E-mail address: joseluis.ayastuy@ehu.eus (J.L. Ayastuy).

https://doi.org/10.1016/j.jece.2022.107612
Received 27 December 2021; Received in revised form 22 February 2022; Accepted 21 March 2022
Available online 23 March 2022

hydrogenation (CTH) by using a hydrogen donor molecule such as methanol, 2-propanol, or 2-butanol [15]. Nevertheless, the formation of by-products and the cost of acquisition and handling of the hydrogen donor can significantly increase process costs [13]. A suitable alternative to circumvent the use of external and non-renewable sources of hydrogen is to carry out glycerol HDO with in-situ produced H_2 via aqueous-phase reforming (APR) of the substrate, in a one-pot reaction.

The present investigation aims to develop a catalytic system that could drive the in-situ generation of hydrogen and its immediate consumption, in the reaction medium, in the HDO reaction. Therefore, a metal-acid bifunctional catalyst is required. In a simple way, the acid function is pivotal for the dehydration reaction whereas the metal function catalyses the hydrogenation reaction [16]. Scheme 1 shows the widely accepted reaction path for the glycerol HDO in liquid phase.

Non-noble metals are less expensive than noble metals and present a greater selectivity towards C-O bond cleavage, and therefore, they are more efficient and economical for 1,2-propanediol production [17]. Transition metals and, more specifically, cobalt-based catalysts, have proved effective in both the production of hydrogen by aqueous-phase reforming (APR) and for glycerol HDO reaction depending on metal–acid/base characteristics [18–20].

Promoters can increase the metal-support interaction, the dispersion of the active metal and can also tune the acid/base characteristics of the catalyst [21]. The addition of a promoter is an economical and time-efficient strategy that can enhance activity [22]. Cerium has been used by several researchers to improve catalyst activity and stability in liquid phase reactions. Its positive effect has been mainly attributed to the existence of oxygen vacancies in the cerium oxide (CeO_2) lattice, which may promote WGS reaction by the activation of the H_2O molecule [23–26]. In addition, its high oxygen mobility can improve hydrothermal stability and avoid the formation of coke precursors [27,28].

In our previous work [29], cobalt-based catalysts were synthesized from cobalt aluminate spinels with different Co/Al molar ratio. These catalysts showed remarkable glycerol conversion and considerable efficiency for C-O cleavage where catalyst with CoAl = 0.625 molar ratio exhibited the most promising performance. Based on that result and known the notable catalytic properties of cerium, in the present work, Ce-modified cobalt aluminate (Co/Al molar ratio = 0.625) catalysts are investigated for the glycerol HDO. In this way, we seek to modify the physico-chemical properties of the pristine catalyst to produce value-added liquid products from glycerol HDO. As far as we know, this type of one-pot synthesized catalysts have not yet been studied in glycerol HDO. The catalytic experiments were carried out in a continuous reactor, where hydrogen was in-situ generated via APR. The synthesized catalysts were thoroughly characterized by several techniques, either in the fresh and reduced form. The various physicochemical properties were correlated with the catalytic performance. In addition, exhausted catalysts were characterized to identify the main deactivation causes.

2. Experimental

2.1. Catalysts synthesis

A series of catalysts based on cobalt aluminate (nominal Co/Al molar ratio = 0.625) doped with cerium were one-pot synthesized by coprecipitation method. In a typical synthesis, an aqueous solution containing $Co(NO_3)_2.6\,H_2O$ (99.999% trace metal basis, Sigma Aldrich), $Al(NO_3)_3.9\,H_2O$ (98% trace metal basis, Fluka) and $Ce(NO_3)_3.6\,H_2O$ (99.999% trace metal basis, Sigma Aldrich) was dropwise added into a beaker containing an aqueous solution of Na_2CO_3 (99.8%, Fluka), under stirring. The synthesis was carried out at room temperature at pH 10, adjusted with NaOH solution (2 M). The resulting suspension was aged at room temperature for 24 h, filtered, washed several times with deionized water, dried overnight at 110 °C in an oven and calcined in a muffle furnace at 500 °C for 5 h (heating at 5 °C/min), in static air atmosphere. The obtained solids were abbreviated xCeCoAl (x: 0, 0.3, 2.1), where x denotes the weight percentage of Ce. As a reference, bare CeO_2 and Co_3O_4 were also synthetized by precipitation, following the same protocol.

2.2. Catalysts characterization

Bulk chemical composition of the solids and metal leaching in catalytic runs were analysed by inductively coupled plasma optical emission spectroscopy (ICP-OES). Textural properties of the solids were obtained from nitrogen adsorption-desorption isotherms at 77 K in a Micromeritics TRISTAR II 3020 equipment. Prior to the adsorption, the samples were outgassed at 300 ºC for 10 h for removing moisture and adsorbed gases. The specific surface area and the main pore size were determined with the BET and BJH (desorption-branch) methods.

XRD spectra were obtained in a PANalytical Xpert PRO diffractometer with $Cu_{K\alpha}$ radiation ($\lambda = 1.5418$ Å). X-ray diffracted radiation was recorded from (2θ values) 20–80º for the powder samples. The identification of the crystal phases was carried by comparison with International Centre of Diffraction Data (ICDD) database. Crystallite size was calculated from the X-ray line broadening analysis using Debye-Scherrer formalism. The lattice parameter (a) of cubic crystal structure was calculated by Eq. 1:

$$a = \frac{\lambda}{2\sin\theta}\sqrt{h^2 + k^2 + l^2} \quad (1)$$

were; θ is the diffraction angle; and h, k and l are the Miller indices.

STEM images were obtained in a FEI Titan Cubed G2 60–300 electron microscope with a high-brightness and a Super-X EDX system under HAADF detector for Z contrast imaging (camera length of 185 mm). The samples were dispersed in ethanol and kept in an ultrasonic bath for 15 min. Afterwards, a drop of suspension was spread onto a TEM copper grid (300 Mesh) covered by a holey carbon film and dryed under vacuum. Particle size distribution was obtained from the statistical analysis of at least 300 particles. The average size of the nanoparticles was calculated from volume to surface ratio (Eq. 2), using ImageJ software:

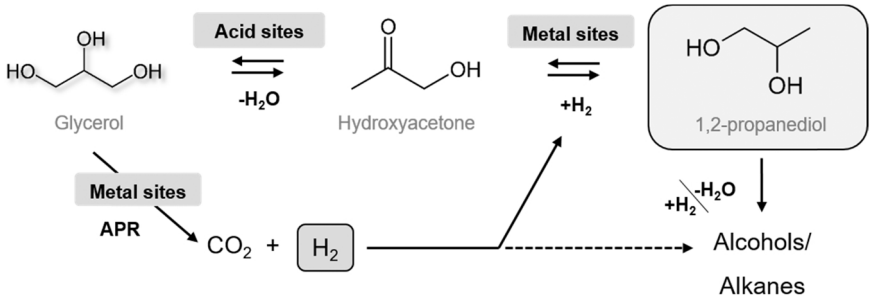

Scheme 1. Reaction path for the glycerol hydrodeoxygenation with in-situ produced hydrogen.

$$< d >= \frac{\Sigma n_i d_i^3}{\Sigma n_i d_i^2} \quad (2)$$

being d_i the diameter of n_i particles.

The oxidation state of the surface elements was analyzed by X-ray photoelectron spectroscopy (XPS) on a SPECS spectrometer with Phoibos 150 1DDLD device, using monochromatic Al Kα (1486.7 eV) X-ray source with 30 eV pass energy at 0.05 eV steps. Samples, previously degassed, were introduced to the ultra-high vacuum analysis chamber (10^{-6} Pa) where the detailed analyses of the elements were performed (time 0.1 s and step energy 30 eV) with an exit angle of 90°. Samples were reduced in-situ, when required. The spectrometer was previously calibrated with Ag (Ag $3d_{5/2}$, 368.26 eV). The BE were calibrated by taking C 1 s peak (284.6 eV) of adventitious carbon as reference. Peaks were deconvoluted after Shirley background subtraction, using a mixed Gaussian Lorentzian function (CASA XPS software).

The UV–vis–NIR DRS spectra were recorded in a Cary 5000 equipment coupled to Diffuse Reflectance Internal (Varian). The reflectance data were converted into absorption by the Kubelka-Munk transformation. The Tauc plots were used to evaluate the difference in the energy of inner electron transitions of the solids. For the calculation, $(\alpha h\nu)^2 vs\ h\nu$ plot was used, where α is the absorption coefficient, ν is the frequency of light and h is the Planck's constant.

^{27}Al Solid State NMR measurements were performed on a 9.4 T Bruker AVANCE III 400 spectrometer operating at resonance frequencies of 104.26 MHz for ^{27}Al. $AlCl_3$ aqueous solution was used as a reference. The spectra were acquired at a spinning frequency of 60 kHz employing a PH MASDVT400W BL 1.3 mm ultrafast probe head. A single pulse of 0.3 μs duration was applied (recycle delay 0.2 s, 36,000 scans).

The reducibility of the calcined samples was analysed by H_2-TPR, carried out in a Micromeritics AutoChem 2920 apparatus. The solid was initially heated in He stream at 550 °C for 1 h to desorb impurities, and then cooled down to room temperature. Then, 5% H_2-Ar flow was passed through the bed containing the sample while temperature was increased up to 950 ºC (heating rate 10 ºC/min) and hold for 1 h. A cold trap was used to prevent water generated by reduction, and reactor exhaust was analysed by Thermal Conductivity Detector (TCD).

Both the hydrogenation and dehydrogenation reactions require metallic function. The number of accessible metallic cobalt atoms was measured by H_2 pulse chemisorption, carried out in a Micromeritics AutoChem 2920 apparatus, at 35 ºC. Samples were previously reduced at 600 °C for 30 min. A chemisorption stoichiometry HCo = 1/1 [30] and a cross-sectional area of 0.0662 nm^2/at_{Co} were assumed [31]. Further information on the metallic function of the catalysts was obtained by measuring their activity in cyclohexane dehydrogenation, which will mainly depend on the metal accessibility [32]. The cyclohexane dehydrogenation was performed over 20 mg of reduced catalysts, in a fixed-bed reactor at 250 ºC and atmospheric pressure, feeding a mixture of anhydrous cyclohexane and hydrogen (1:3000 mol ratio). The gas product (benzene and cyclohexane) were online analysed by GC (column Al_2O_3-KCl, HP) coupled to a flame ionization detector (FID).

The amount and strength of surface acid sites of the reduced catalysts were measured by means of NH_3-TPD and isomerization of 3,3-dimethyl-but-1-ene (33DM1B) model reaction. For ammonia chemisorption/desorption experiments (Micromeritics AutoChem 2920 equipment) a series of 10% NH_3-He pulses were introduced at 90 ºC, until saturation. Subsequently, the sample was exposed to He flow for 60 min to remove reversibly bound NH_3. Finally, the temperature was raised to 950 °C (heating rate 5 °C/min) with continuous ammonia monitoring. The total acidity was calculated from the integration of the pulses, and the strength of the acid sites was evaluated from the corresponding TPD profile. The model reaction of skeletal isomerization of 33DM1B was used to characterize the Brønsted acid sites, since Lewis acid centers are not involved in this reaction [33]. The catalyst (100 mg) was in-situ reduced, and cooled down to the reaction temperature (300 °C) under inert flow. The 33DM1B partial pressure and flow rate were set at 20 kPa and 15.2 mmol/h, respectively. The obtained products were online analysed by GC-FID on a RTx-1 (Restek) column.

The characterization of the carbonaceous deposits in the spent catalysts was carried out by Raman spectroscopy (Renishaw InVia Raman spectrometer, Leica DMLM microscope) using 514 nm laser. The power density of the laser beam was reduced in order to avoid the photodecomposition of the samples. In order to improve the signal to noise ratio, 40 s were used for each spectrum and 10 scans were accumulated at 10% of the maximum power of the 514 nm laser, in the 1000–2000 cm^{-1} spectral window.

Carbonaceous deposits on spent catalysts were quantified by Temperature Programmed Hydrogenation (TPH) in a Setaram Setsys Evolution thermobalance coupled to a Mass Spectrometer (Pffeifer Vacuum OmniStar) following the evolution of $m/z = 15$ (CH_4) signal. First, sample was cleaned under a He flow, at 550 °C for 1 h in order to remove absorbed organics. After cooled down to 40 °C, 5%H_2/Ar flow was passed through the sample heated at 10 °C/min up to 900 °C.

2.3. Catalytic performance

Catalytic performance was evaluated in a bench-scale fixed-bed upflow reactor (Microactivity Effi, PID Eng&TEch) with synthetic aqueous solution of glycerol (10 wt% glycerol) at 260 ºC/50 bar, operating at WHSV= 24.5 h^{-1}. About 0.5 g of catalyst, particle size of 0.04–0.16 mm, were mixed with deactivated quartz wool and in-situ reduced under 10% H_2/He flow at 600 ºC and atmospheric pressure, for 1 h. The reactor was pressurised with He and when the desired pressure was achieved, the He flow was switched to bypass, and the glycerol solution (0.2 mL/min) was fed to the reactor while the temperature was progressively raised up to the reaction temperature, at 5 ºC/min. Catalytic performance was measured at 3 h TOS (time on stream). Zero time was taken when reactants reached the catalyst bed, once the reaction temperature was reached. Gaseous and liquid phases were separated at 5 ºC in a Peltier device. The gaseous products were swept away with a He flow (40 mL/min) applied immediately after the backpressure regulator. Product distribution was online analysed by a μGC (Agilent) equipped with four columns (Al_2O_3-KCl, PPQ and MS5A columns that used He as a carrier, and MS5A column which used Ar as a carrier). The liquid product was collected every hour in 2 mL glass vials and off-line analysed by GC-FID (Agilent, 6890N) and HPLC-RI (Waters, Hi-Plex H column). The quantification of liquid compounds was performed by external calibration. Total organic carbon (TOC) in the liquid phase was measured on a Shimadzu TOC L apparatus. The carbon balance was 96% ± 5 for all the experiments. After catalytic test, spent catalyst was recovered and characterized by a sort of techniques.

The catalytic performance was calculated according to the following indices. The total glycerol conversion (X_{Gly}) was calculated as:

$$X_{Gly}(\%) = 100 \times \frac{F_{Gly}^{in} - F_{Gly}^{out}}{F_{Gly}^{in}} \quad (3)$$

where F_{Gly}^{in} and F_{Gly}^{out} are the glycerol molar flow at the reactor inlet and outlet, respectively.

The carbon yield to liquid (X_{liq}) is the ratio of the total moles of carbon in the liquid products to the moles of carbon fed:

$$X_{liq}(\%) = 100 \times \frac{\sum_{i=m}^{n} F_{Catoms,liq}^{out}}{3F_{Gly}^{in}} \quad (4)$$

yield (Y_i) and selectivity (S_i) of liquid product i were calculated on the basis of carbon molar flow of i product in liquid phase, as follows:

$$Y_i(\%) = 100 \times \frac{F_{Catoms,i}^{out}}{3F_{Gly}^{in}} \quad (5)$$

$$S_i(\%) = 100 \times \frac{F^{out}_{Catoms,i}}{3F^{in}_{Gly} \cdot X_{Gly}} \quad (6)$$

Selectivity to alkanes (S_{alk}) was calculated on the carbon basis, as follows:

$$S_{alk}(\%) = 100 \times \frac{\sum_{n=1}^{3} n \cdot F^{out}_{C_nH_{2n+2}}}{3F^{in}_{Gly} \cdot X_{Gly}} \quad (7)$$

While the overall selectivity to liquid products accounts the total C atoms in liquid phase, excluding unreacted glycerol.

$$S_{liq}(\%) = 100 \times \frac{\sum_{i=m}^{n} F^{out}_{Catoms,i}}{3F^{in}_{Gly} \cdot X_{Gly}} \quad (8)$$

Hydrogen yield (Y_{H2}) is the ratio between the molar flow of hydrogen produced and the theoretical one according to the glycerol fed to the reactor.

$$Y_{H2}(\%) = 100 \times \frac{F^{out}_{H2}}{7 \cdot F^{in}_{Gly}} \quad (9)$$

The degree of oxygen removal (DOR) was defined as the ratio of the removed oxygen atoms in the liquid phase to the initial molar flow of oxygen.

$$DOR(\%) = 100 \times \frac{F^{in}_{Oatoms} - \sum_{i=m}^{n} F^{out}_{Oatoms,i}}{F^{in}_{Oatoms}} \quad (10)$$

3. Results

3.1. Bulk chemical composition and textural properties

Table 1 lists the bulk chemical composition and textural properties of the synthesized solids. Actual metal content measured by ICP-OES revealed a good agreement with the nominal Ce content (variation less than 3%) and Co/Al ratio (slightly higher than nominal).

The isotherms of all the calcined solids (Fig. 1A) were IV type, which were characteristic of mesoporous materials, with the P/P_0 position of the inflection point (around 0.5) corresponding to a mesoporous range diameter. The hysteresis loop shape suggested randomly distributed mesopores formed by nanoparticle assembles. Regarding the BJH pore size distribution of the solids, it varied with Ce content (Fig. 1B). While pristine 0CeCoAl and 0.3CeCoAl presented a unimodal PSD with maximum at 6.8 nm sized pore, sample 2.1CeCoAl presented a bimodal distribution with pores at 7.8 nm and 13 nm, which would anticipate a certain ceria segregation in the later assay. The surface area, pore volume and average pore size of the solids are shown in Table 1. Pristine 0CeCoAl showed $S_{BET} = 125.3\ m^2/g$, which was slightly lower than stoichiometric $CoAl_2O_4$ (about $150\ m^2/g$) [29]. Recall that 0CeCoAl solid had more Co than stoichiometric (CoAl = 0.625 vs. 0.5), in form of Co_3O_4, characterized by its low surface area [34]. Coprecipitation of Ce together with Co and Al leaded to an increase by 16–18% in the S_{BET} as compared to 0CeCoAl counterpart. Likewise, an increase in pore volume was observed (between 22% and 33% increase) for Ce-doped solids.

After reduction (at 600 °C, 2 h), the isotherms were also of IV type.

Table 1
Cerium content and textural properties of Ce-doped solids.

Catalyst	Ce (wt %)	Co/Al (at./at.)	S_{BET} (m^2/g)	V_{pore} (cm^3/g)	d_{pore} (nm)
0CeCoAl	0	0.634	125.3 (101.7)	0.280 (0.375)	6.8 (9.6)
0.3CeCoAl	0.29	0.637	148.1 (138.3)	0.341 (0.403)	6.7 (8.7)
2.1CeCoAl	2.15	0.640	146.4 (131.8)	0.371 (0.423)	7.9 (9.7)

In parenthesis, the values for the fresh reduced solids

The specific surface area of Ce-doped solids slightly dropped (by 7–10%) as compared to calcined counterparts, with a concomitant increase in the mean pore size values (increase by 14–18%). It should be noted that this increase was much less pronounced than that revealed by 0CeCoAl sample (41%). Decrease in the S_{BET} in the reduced solids was attributed to the dilution effect by metallic cobalt in the solid surface. Compared to 0CeCoAl assay, S_{BET} of xCeCoAl reduced samples was 30–36% higher. Therefore, up to this point, we can conclude that the addition of Ce notably improved the textural properties of the solid in both calcined and reduced conditions, acting as structural promoter.

3.2. Nature and morphology of the phases

XRD diffractograms of Ce-doped and pristine cobalt aluminate solids, in their calcined and reduced forms, are displayed in Fig. 2. All the calcined samples exhibited the characteristic peaks for spinel phase. It should be noted that the Co/Al ratio in our catalyst was 0.64 which is around 30% larger than the stoichiometric ratio in $CoAl_2O_3$ (i.e. CoAl = 0.5). Thus, the segregation of part of Co atoms to form Co_3O4 was expected to occur. The formation of $CoAl_2O_4$ spinel phase occurs due to the counter-diffusion of $Co^{\delta+}$ and Al^{3+} ions at the interface between Al_2O_3 and Co_3O_4 oxides, both isotopic crystal structures, formed at the early stages of the thermal treatment [35]. Unfortunately, it was difficult to differentiate between Co_3O_4 and $CoAl_2O_4$ by XRD analyses due to the similarities in the crystal structure and D-spacing (PDF 00–042–1467 and PDF 00–044–0160, respectively). Diffraction patterns of Ce-doped solids were almost the same as that of pristine 0CeCoCAl, indicating that the solid retained the same crystal structure upon Ce doping. Moreover, the spinel peaks became narrower upon Ce addition (inset in Fig. 2A), indicating increase in the crystallite size. Only the catalysts with the highest Ce content showed diffraction peaks at 28.7° and 48.3° (2θ) attributed to CeO_2 in its cerianite-phase structure (PDF 00–034–0394), indicating segregation of Ce. The broadness of its characteristic XRD peaks suggested small size of the ceria crystallites. This peak was not observed for sample 0.3CeCoAl, which confirmed that for that solid, Ce ions were substituted in the spinel lattice. According to literature, the cerium solubility into spinel phase is CeCo = 0.03 molar ratio [36]. In our 2.1CeCoAl solid, the actual Ce/Co ratio was 0.025, close to the solubility limit. A careful inspection of (311) peak of the spinel phase showed a slight downshift in its position (inset of the Fig. 2), indicating that the addition of Ce caused a distortion in the spinel structure. Accordingly, Ce-doping generated a growth in the spinel lattice parameter (Table 2), which was attributed to the larger ionic radius of Ce^{4+} ions (101 pm) as compared to Co^{2+} (79 pm), Co^{3+} (69 pm) and Al^{3+} (67.5 pm) host ions. Similar features were obtained by others [37].

The intensity ratio of the (220) to (440) diffraction planes, indicative of the cobalt ions in tetrahedral to octahedral sites [38], increased as Ce-content augmented (Table 2), indicating a preferential arrangement of cobalt ions in tetrahedral coordination [39]. The mean crystallite size of spinel phase (without distinction between $CoAl_2O_4$ and Co_3O_4) increased between 28% and 40% with Ce doping. The average crystallite sizes of segregated ceria phase could not be determined due to its weak signal. Undoubtedly, lattice changes would affect spinel structure.

After reduction, diffraction peaks of spinel phase remained (Fig. 2B), indicating that the reduction temperature was not enough for complete reduction of all cobalt species. Upon reduction, diffraction peaks assignable to metallic Co emerged in all samples, whereas in sample 2.1CeCoAl, the formation of an alloy-like Ce_5Co_{19} rhombohedral phase (PDF 026–1084) more stable structure was observed. The formation of this stable phase would explain the shift at higher temperatures of peaks III and IV observed in the H_2-TPR study (see below). The mean crystallite size of metallic Co of Ce-doped catalysts (Table 2) were notably smaller than that of the pristine 0CeCoAl assay. It could be concluded that, Ce insertion in the cobalt aluminate spinel structure, strengthens the metal-support interaction in the reduced catalyst and contributes to a decrease of Co^0 particles size.

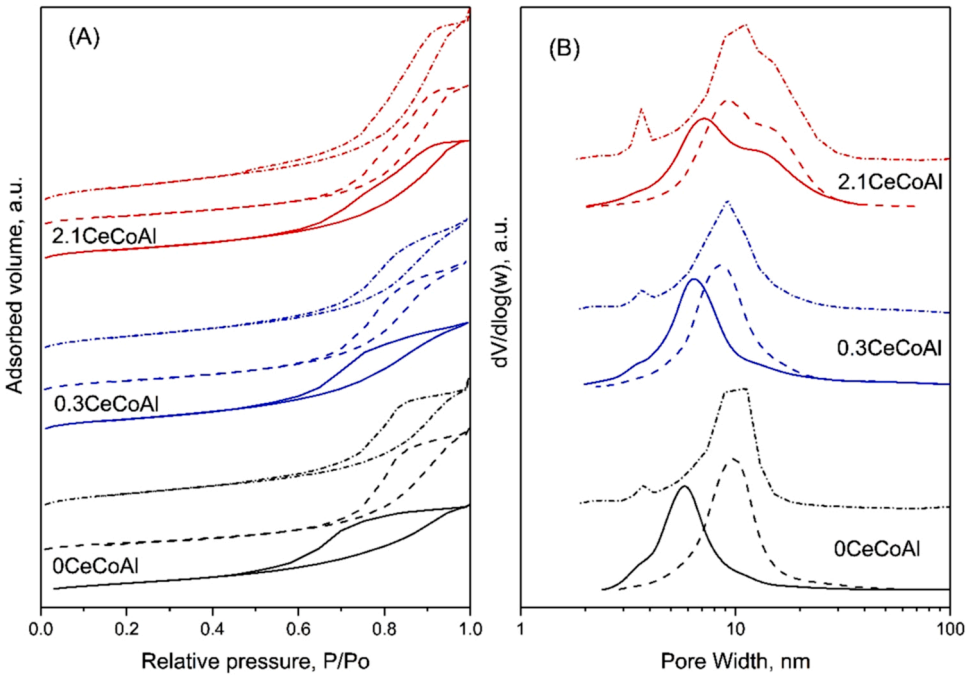

Fig. 1. Nitrogen adsorption-desorption isotherms (A) and pore size distribution (B) of the calcined (solid lines), reduced (dashed lines) and used (dash-dotted lines) materials.

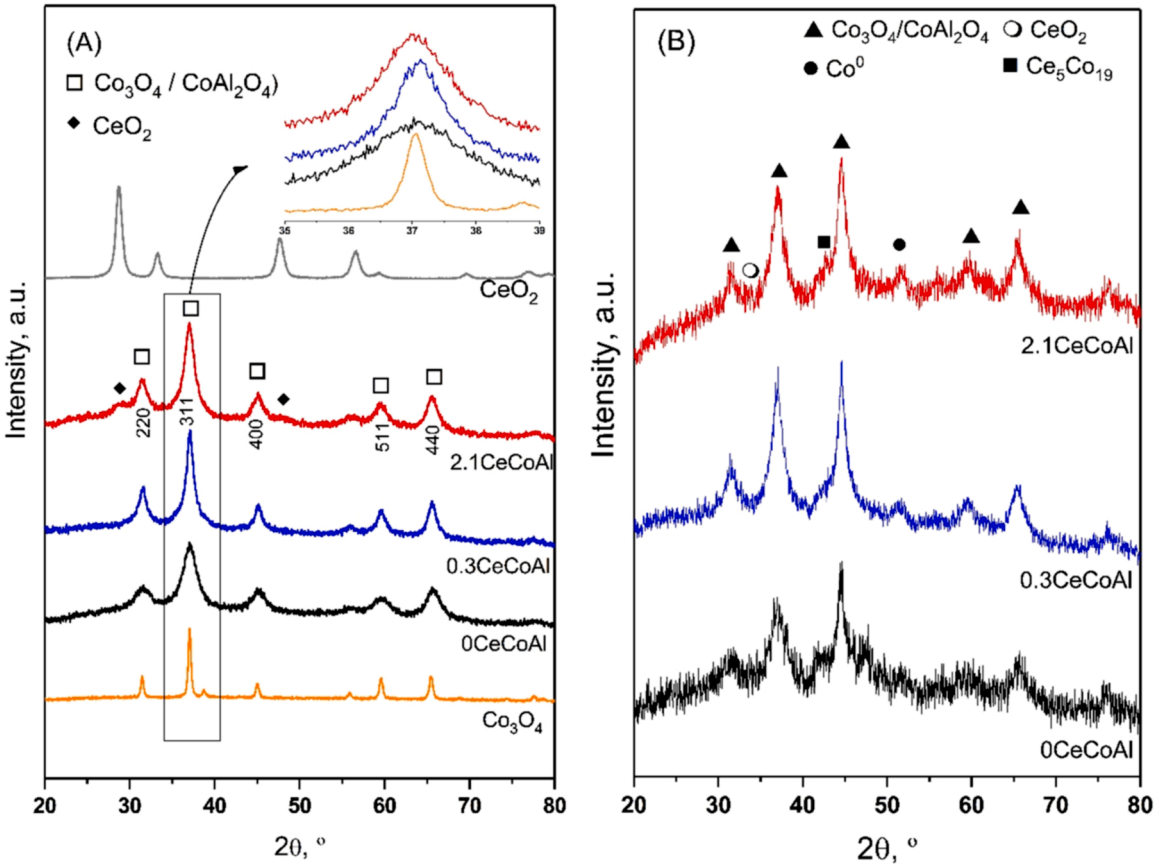

Fig. 2. XRD patterns of (A) calcined and (B) reduced xCeCoAl solids. The inset in the figure: enlarged (311) diffraction peak.

The morphology of the reduced materials was analysed by STEM micrographs. The obtained micrographs and the resulting particle size distribution histograms are depicted in Fig. 3. The chemical composition of the nanoparticles was also confirmed by EDX analysis. Cobalt nanoparticles (mixture of cube and cuboid shapes) in Ce-doped catalysts were homogenously distributed, as were the tiny cerium nanoparticles that

Table 2
XRD results of the calcined and reduced xCeCoAl solids.

Sample	Calcined form			Reduced form
	d_{spinel} (nm)	a_{spinel} (nm)	I_{220}/I_{440}	d_{Co^0} (nm)
0CeCoAl	5.0	0.8040 ± 0.0014	0.63	16.5
0.3CeCoAl	6.4	0.8055 ± 0.0014	0.71	9.8
2.1CeCoAl	7.0	0.8059 ± 0.0018	0.76	7.2

were found completely scattered throughout the samples. Ce-rich domains were observed for 2.1CeCoAl assay, indicating some Ce-rich phase. Co^0 particle size was measured by imageJ software, and a similar mean diameter (ca. 20 nm) was measured for all catalysts, suggesting they are composed by agglomerates of smaller crystallites. Regarding the particle size distribution, particle size ranged between 10 and 26 nm while 75% of the nanoparticles were smaller than 20 nm. Ce-modified solids showed a broader distribution curve, in line with the Co^0 crystallite sizes evaluated by XRD (0.3CeCoAl: 9.8 nm; 2.1CeCoAl: 7.2 nm).

3.3. Structure and coordination state

XPS spectroscopy was employed to examine the oxidation state and the surface composition of xCeCoAl solids. The BE of the photoelectron peaks for both calcined and reduced samples are summarised in Table 3. The high-resolution XPS spectra for Co, Ce and Al in the calcined solids are shown in Fig. S1 (Supporting Information). It can be seen that the spin-orbit splitting (ΔBE) between Co $2p_{3/2}$ and Co $2p_{1/2}$ peaks was 15.21 eV for 0CeCoAl, which increased to 15.67 eV at the lowest Ce loading (0.3CeCoAl). Further increase in Ce doping decreased the ΔBE (i.e. 15.35 eV for sample 2.1CeCoAl). The satellite peak of Co $2p_{3/2}$ is located at approximately 4–5 eV higher BE than the main Co $2p_{3/2}$ peak, which is characteristic of Co^{2+} in $CoAl_2O_4$ framework [40,41]. In the Al 2p region, both the calcined and reduced samples show peaks at around 74 eV which can be assigned to Al^{3+} cations bonded with oxygen. The peaks could be deconvoluted into octahedral and tetrahedral Al^{3+} contributions, being the former at higher BE [42]. All the solids had mainly octahedral Al^{3+}. In addition, in the fresh catalysts Co $2p_{3/2}$ band appeared shifted to lower binding energies as Ce loading increased, what suggested a stronger interaction between elements in Ce-doped solids, in agreement with H_2-TPR results.

Ce 3d peaks of the calcined solids (Fig. S1C, Supporting information) showed a $3d_{3/2}$ and $3d_{5/2}$ separation of around 18.2 eV, in good agreement with literature [43–45]. Unambiguously, no characteristic peaks of tetravalent Ce^{4+} were detected. Instead, characteristic peaks of Ce^{3+} were observed at around 902.7 ± 0.5 eV and 885.2 ± 0.7 eV. The

Table 3
XPS analysis results for xCeCoAl (BE in eV).

Catalyst	Al 2p	Co $2p_{3/2}$		Ce $3d_{5/2}$	Surface Co/Al
		Co^{2+}	Co^0	Ce^{3+}	
0CeCoAl	75.6 (74.2)	781.6 (781.3)	(778.0)	n.a.	0.266 (0.139)
0.3CeCoAl	74.2 (74.2)	781.3 (781.8)	(778.7)	884.6 (885.9)	0.223 (0.213)
2.1CeCoAl	74.0 (73.9)	781.8 (782.1)	(779.1)	885.0 (884.5)	0.243 (0.207)

Value in parenthesis corresponded to reduced samples.

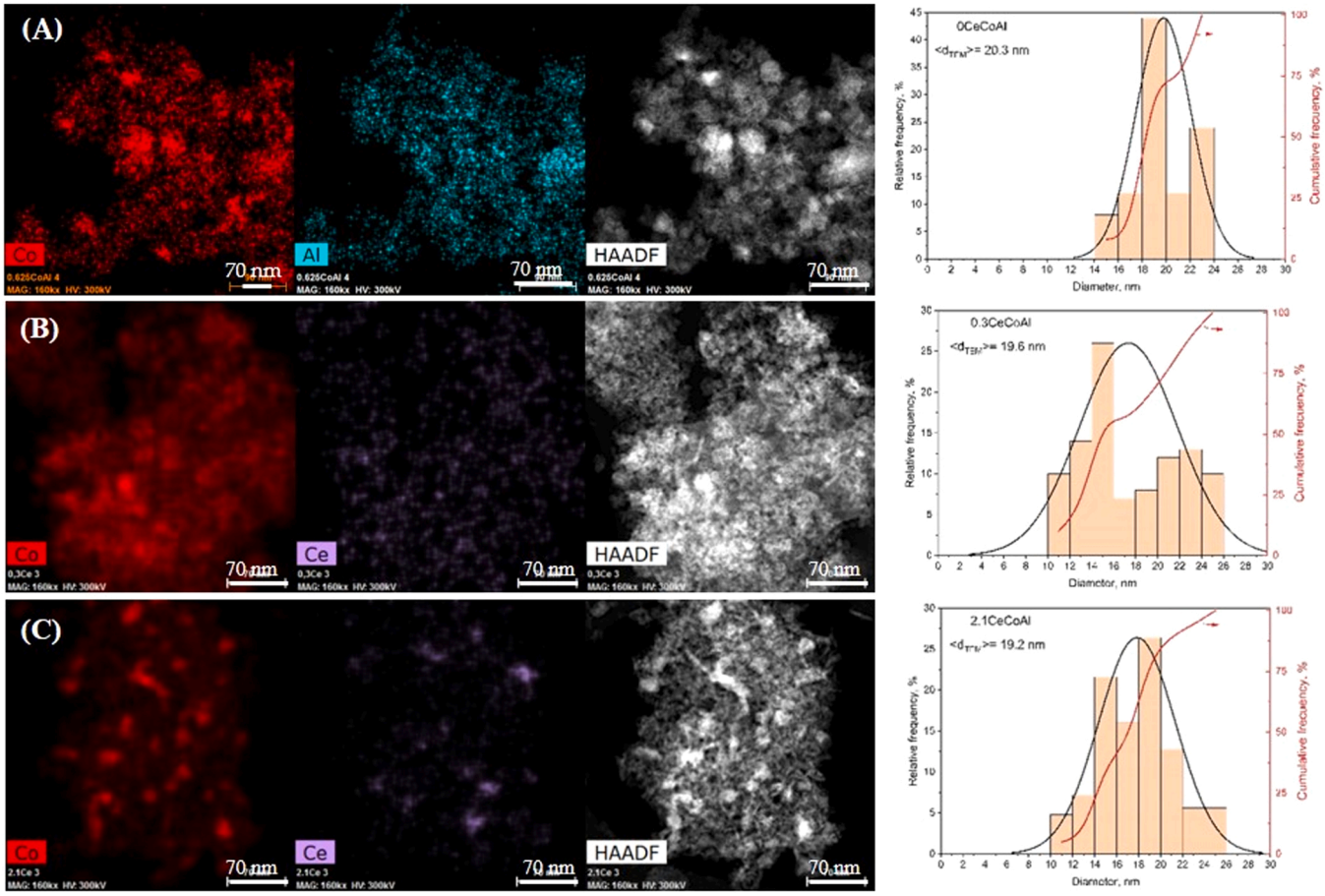

Fig. 3. STEM micrographs and Co^0 particle size distribution of reduced catalysts: (A) 0CeCoAl, (B) 0.3CeCoAl, (C) 2.1CeCoAl.

latter result of Ce $3d^9 4f^1$ O $2p^6$ final-state [43].

The Co 2p XPS spectra of the reduced solids are displayed in Fig. 4. The most striking difference was the signal from metallic cobalt, absent for calcined solids. It appeared at 778.0 eV for 0CeCoAl catalyst and shifted to higher BE for samples xCeCoAl ($\Delta E = 0.7–1.1$ eV), in agreement with their lower band gap energies. In addition, for the reduced xCeCoAl, deconvolved Co^0 peak were less intense than for 0CeCoAl catalyst, in agreement with H_2-TPR results.

Two typical bands could be observed in the O 1s XPS spectrum of the reduced samples (Fig. S1D, Supporting Information). The peak at 530.9–531.6 eV corresponded to adsorbed oxygen (O_{ads}) species and the other, located at lower BE coincided with surface lattice oxygen (O_{latt}) [46]. O_{ads} species has greater mobility than O_{latt}, and are considered responsible for maintaining the charge balance in the structure [47,48]. The ratio O_{ads}/O_{latt} significantly decreased after Ce loading (1.07–1.51 vs. 3.34) what implied a decrease in oxygen vacancies.

A quantitative evaluation of the chemical composition of Co and Al at solid surface was done for both the calcined and reduced samples (Table 3). It is interesting to note that surface Co/Al ratio was lower than the bulk ratio measured by ICP-OES which was around 0.63 for all catalyst. This enrichment in Al could be attributed to its lower surface energy in comparison to Co [49], which generated cobalt-deficient aluminium-rich phase on the surface. Also, note that upon reduction, the Co/Al ratio decreased by half for the non-doped reference catalyst, whereas it remained constant for Ce-doped samples. The smaller metallic Co particle sizes of the later could be involved in preserving the Co/Al ratio at the surface.

Fig. 5 shows the UV–vis DRS spectra of the calcined catalysts. Bare CeO_2 sample, used as reference, showed two absorbance bands below 400 nm. Bands at 257–278 nm can be attributed to O^{2-}-Ce^{4+} charge transfer transitions involving Ce^{3+} (≈255 nm) and Ce^{4+} ions (≈278 nm) with different coordination numbers, whilst a characteristic vibration of interband transitions at 328 nm was observed [50]. The spectrum of 0CeCoAl sample was very similar to bare Co_3O_4, with a small blueshift of the bands corresponding to tetrahedrally coordinated Co^{2+} ions, indicative of Co-Al interaction [29,51]. Thereby, 0CeCoAl shows features from tetrahedral Co^{2+} (d–d transition bands at 1210, 1330 and 1500 nm; d–d absorption bands at 558, 585 and 621 nm) [52]. On the other hand, Ce-doped solids exhibited two broad bands in the UV region centred at around 420 and 635–644 nm and characteristic cobalt aluminate bands in the NIR region (1200–1500 nm). These bands were found to be less intense than those shown by pristine 0CeCoAl assay with a slight band shift from 1420 to 1460 nm, indicative of Ce incorporation to spinel.

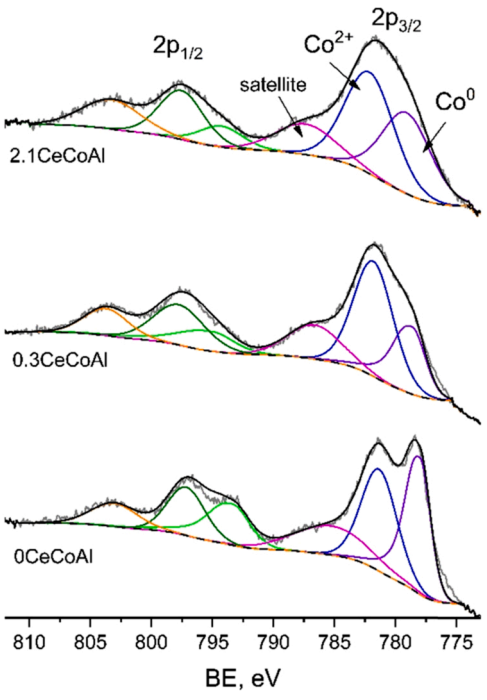

Fig. 4. Detailed Co 2p XPS spectra of reduced xCeCoAl solids.

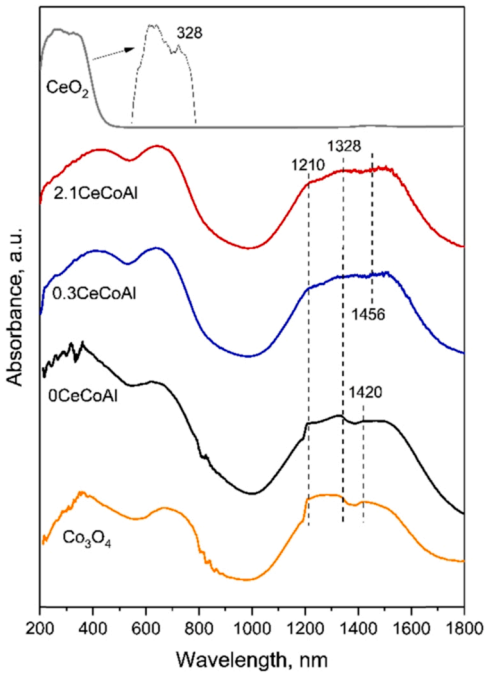

Fig. 5. UV vis DRS spectra of calcined Ce-doped solids.

The direct band gap (E_g) for all samples was estimated by Tauc plot (Fig. S2, Supporting Information). Typically, E_g corresponds to a ligand-to-metal charge transfer excitation energy, and shows the tendency of adjacent transition-metal centers to gain electron density [53]. A band gap of 1.38 eV was estimated for pristine 0CeCoAl solid and decreased to 0.81 and 0.48 eV for samples with 0.3% and 2.1% of cerium, respectively. The lowering of E_g for Ce-doped samples could be attributed to the incorporation of metal cations into the framework of spinel crystal [54]. The distortion caused in the cell could act as trapping-centers to capture electrons [55].

Fig. S3 (Supporting information) shows the ^{27}Al NMR spectra obtained from the reduced solids. Catalyst 0CeCoAl shows an asymmetric single peak, at 2 ppm, corresponding to octahedral aluminium. A subtle signal at around 60 ppm, corresponding to tetrahedral aluminium, could be also deduced [56]. Ce-doping caused a slight shift of main peak to the right, and the appearance of a bulge in the 25–40 ppm range, which can be ascribed to five-coordinated aluminium. Both features indicated an increase in the disorder degree in the Ce-containing solids [57], in agreement with XRD results.

3.4. Reducibility of the solids

Fig. 6 displays the H_2-TPR profiles of xCeCoAl solids. Those of bulk Co_3O_4 and CeO_2 (5 times magnified) are also displayed as a reference. The reduction profile of bulk Co_3O_4 comprised two well defined reduction bands with maximum at 300 °C and 425 °C, and ascribed to $Co^{3+} \rightarrow Co^{2+}$ and $Co^{2+} \rightarrow Co^0$ reduction steps, respectively [58]. Bare CeO_2 also showed two main reduction bands: the low temperature peak, centred at 496 °C, can be ascribed to the reduction of surface caps of ceria whereas the high temperature peak, centred at 845 °C, can be ascribed to the reduction of the innermost layers (bulk) of the ceria [59].

The reduction of the pristine 0CeCoAl [29] started at around 150 °C. Four reduction peaks could be identified. Peak I (at 292 °C) was ascribed

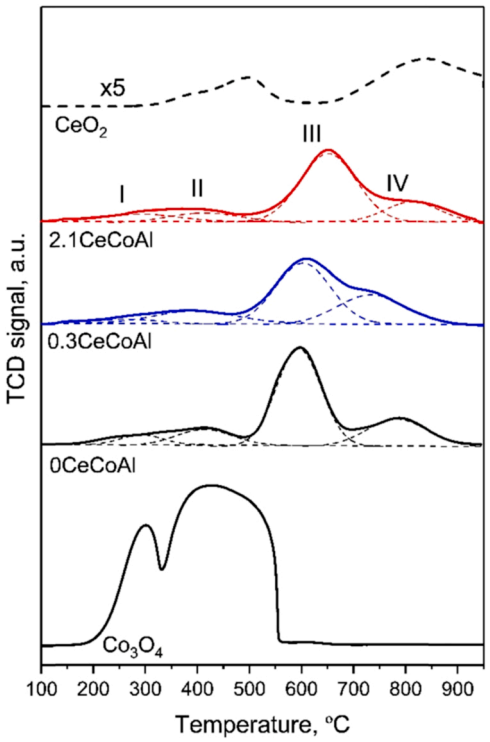

Fig. 6. H_2-TPR profiles of spinels samples modified by cerium.

to $Co^{3+} \rightarrow Co^{2+}$ reduction of the surface cobalt cations without any interaction with the alumina or cobalt aluminate phases. Peak II (at 413 °C) was also attributed to the reduction of Co^{3+} species though in close interaction with alumina or cobalt aluminate [29,60]. The reduction peak at 594 °C (peak III) was assigned to $Co^{2+} \rightarrow Co^0$. Finally, peak IV (at 783 °C) was assigned to the reduction of cobalt ions in the stoichiometric cobalt aluminate ($CoAl_2O_4$) phase [29,61]. The XRD signals from Co_3O_4 and $CoAl_2O_4$ are consistent with the peak assignment in H_2-TPR measurement. It is interesting to note that the strong interaction between the cobalt ions and the support (mixture of alumina and cobalt aluminate) notably hindered both $Co^{3+} \rightarrow Co^{2+}$ and $Co^{2+} \rightarrow Co^0$ reduction stages. Therefore, peak III from 0CeCoCe assay significantly upshifted (by 159 °C) as compared with bare Co_3O_4. This behaviour reflects the lower reducibility of $Co^{\delta+}$ species in the Ce doped assays and is in line with XPS data where BE of Co $2p_{3/2}$ decreased with Ce loading in the calcined series.

In the Ce-doped samples, due to the low amount of CeO_2 added, its reduction peaks were overlapped by the most intense cobalt reduction peaks. As for catalyst 0CeCoAl, Ce-doped samples showed four reduction peaks. After addition of a small amount of Ce (0.3 at%), peaks I and II, ascribed to $Co^{3+} \rightarrow Co^{2+}$, shifted to lower temperatures indicating a promotional effect of ceria on the partial reduction of both kinds of Co^{3+}. However, such promotional effect was not observed in catalyst 2.1CeCoAl (see Table 4). Peak III (reduction of Co^{2+} to Co^0) appeared at higher temperatures than those exhibited by 0CeCoAl, probably due to the hardening of Co-O-Al bonds because of the presence of electron trapping sites. Finally, the reduction of cobalt species in $CoAl_2O_4$ phase (peak IV), was again favoured at small Ce doping whereas in 2.1CeCoAl it took place at the highest temperature (813 °C, 30 °C higher than that of 0CeCoAl). This higher temperature requirement led to a lower degree of reduction of this sample after the activation process carried out before the catalytic experiments (reduction at 600 °C). Overall, Ce-modified solids would achieve a smaller reduction than pristine 0CeCoAl, especially 2.1CeCoAl, worsened by the formation of Ce_5Co_{19}.

Table 4 shows the results of H_2-TPR analysis. Strictly speaking, H_2 consumption due to ceria reduction should be subtracted. However, the maximum theoretical H_2 consumption expected from ceria reduction in sample 2.1CeCoAl was 0.076 $mmol_{H2} \cdot g^{-1}$, what represented 1% of the total H_2 uptake. Thus, the total H_2 consumption is given.

Table 4
H_2-TPR analysis results of Ce-containing samples.

Sample	H_2 uptake ($mmol_{H2}/g$)					Degree of reduction[a] (%)
	Total	Peak I	Peak II	Peak III	Peak IV	
0CeCoAl	7.04	0.392 (292)	0.881 (413)	4.407 (594)	1.360 (783)	62.6
0.3CeCoAl	7.05	0.371 (262)	0.997 (395)	3.572 (603)	2.110 (734)	60.2
2.1CeCoAl	7.09	0.498 (295)	0.787 (414)	4.582 (652)	1.223 (813)	45.9

In parenthesis the temperature of the peak (in °C).
[a] H_2 uptake at 600 °C with respect to that at 950 °C.

3.5. Metallic function characterization

The amount of exposed metal, calculated by isothermal H_2 pulse chemisorption, is gathered in Table 5. Consistent with the reducibility results discussed above, Ce addition remarkably decreased the available cobalt. This depletion was around 36% at the lowest Ce loading, and reached up to 44% at 2.1% Ce.

The activity of catalysts in the cyclohexane dehydrogenation model reaction was measured in terms of TOF values (Table 5). Measured values clearly indicate a higher activity of surface atoms in Ce-doped samples. The activity in cyclohexane dehydrogenation, expressed as TOF_{dehyd}, increased between 42% and 52% for 0.3CeCoAl and 2.1CeCoAl catalysts respect to non-doped catalyst. UV–vis DRS analysis revealed differences in the inner electron transitions of the solids. Also, Ce-doped catalysts had smaller Co^0 crystallites than pristine 0CeCoAl. Both features modified the metal-surroundings interaction, which could affect the intrinsic activity of cobalt in cyclohexane dehydrogenation. Moreover, the higher intrinsic activity of Ce-doped catalysts is also a desirable characteristic for activating H_2 molecule in hydrogenolysis reactions.

3.6. Acid function characterization

The surface acid site density of the reduced solids is summarised in Table 5, and the strength distribution, according to the desorbed NH_3 profiles, is displayed in Fig. S4 (Supporting Information). The acid site strength were categorized according to their desorption temperatures, as follows: weak (desorption temperature range 90–300 °C), medium (300–650 °C) and strong (> 650 °C), while the percentage contribution of each strength site was estimated from the area under ammonia desorption profile. Ce-doping led to an increase in the density of surface acid sites (increase by 55–72%) and a change in the distribution of the acid strength. Ce-doped solids exhibited a higher density of medium and strong acid centers compared to their counterpart 0CeCoAl assay. In percentage terms, strong acid sites increased from 8.1% for sample 0CeCoAl to 26% for both Ce-containing samples. Morterra et al. [62] found that Ce-doped alumina had more acidity than parent γ-alumina, and ascribed this to the modified environment of Al^{3+} cations by cerium. In fact, ^{27}Al NMR and UV–vis DRS results pointed to this.

Table 5
Characterization of the metallic and acid functions of xCeCoAl catalysts.

Sample	Exposed Co^0 (at./g)	TOF_{dehyd} (s^{-1})	Acid sites density ($\mu mol_{NH3}/m$)	$A_{isom,0}$ ($\mu mol/m^2 \cdot h$)
0CeCoAl	$23.0 \cdot 10^{18}$	0.59	0.51	2.8
0.3CeCoAl	$14.6 \cdot 10^{18}$	0.84	0.79	252
2.1CeCoAl	$12.9 \cdot 10^{18}$	0.90	0.88	191

Cobalt aluminate is characterized by having Lewis acidity rather than Brønsted acidity [63]. Thus, it is expected the Lewis acid centers to prevail in Ce-doped solids. In glycerol APR conditions, dehydration of primary or secondary hydroxyl from glycerol depends on the abundance of Lewis or Brønsted acid sites [64]. Therefore, it was considered useful to evaluate the Brønsted acidity of the catalysts. Evaluation of Brønsted acidity was done in terms of the activity in the skeletal isomerization of 33DM1B. Table 5 showed large differences between 0CeCoAl and Ce-doped catalysts. Both Ce-containing catalysts were 70–90 times more active for skeletal isomerization of 33DM1B, indicating their acid sites had more acid Brønsted characteristics than 0CeCoAl, probably linked to their higher penta-coordinated Al content. In conclusion, the total acid sites density increased with Ce, which is a key feature to protonate the hydroxyl groups before oxygen loss as water.

3.7. Catalytic performance in glycerol HDO

The Weisz-Prater and Mears criteria (Table S1, Supporting Information) was used to confirm the absence of mass-transfer limitations in catalytic experiments. Blank tests carried out with the reactor bed filled solely with quartz wool (used to support the catalyst inside the reactor) showed no glycerol conversion, which suggested that homogeneous APR had no contribution to the catalytic conversion of glycerol. Similarly, HDO reaction with calcined 0CeCoAl catalyst resulted in almost null conversion, which indicated that metallic function was required for the HDO reaction. Furthermore, catalytic experiments with reduced cobalt oxide (Co_3O_4) resulted in low liquid yield [29], indicating the acid sites are involved in the production of liquids.

The catalytic performance in the glycerol HDO without external addition of hydrogen was studied in a continuous fixed bed reactor feeding a solution of 10 wt% glycerol/water, at WHSV of 24.5 h^{-1}, during 3 h TOS. The results expressed as glycerol conversion, carbon yield and selectivity to liquids are shown in Fig. 7.

Catalyst 0CeCoAl [29] exhibited higher glycerol conversion (95.7%) than Ce-doped catalysts. Among Ce-modified catalysts, that with the lowest cerium load showed slightly higher glycerol conversion (X_{gly}= 60.0% for 0.3CeCoAl vs 55.0% for 2.1CeCoAl). The low glycerol conversions obtained with Ce-containing catalysts might be related to the stabilizing effect of cerium on the Co^{2+} ion, delaying its reduction to Co^0, as seen by H_2-TPR analyses. Furthermore, and related to the above, available metallic area was lowered for Ce-doped catalyst.

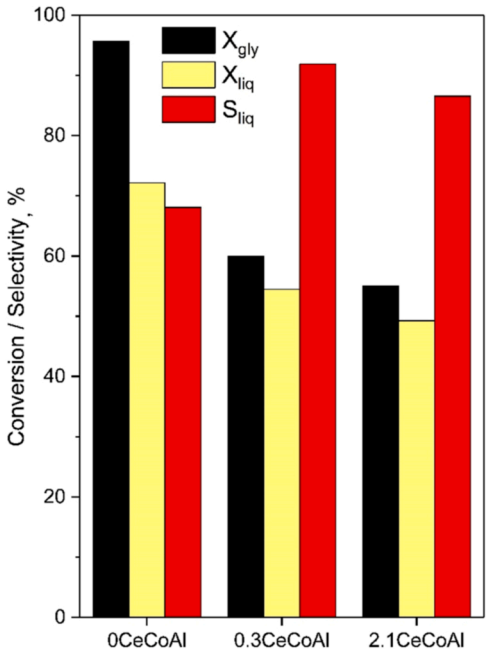

Fig. 7. Effect of doping Ce over cobalt aluminate spinels on glycerol hydrogenolysis.

Carbon yield to liquid (X_{liq}) was also markedly lowered for Ce-containing catalysts, and decreased with increasing dopant loading. This trend is intrinsically linked with the glycerol conversion presented for these samples. Nevertheless, selectivity towards liquid products improved by 34.5% with the addition of 0.3% Ce and by 27.1% on 2.1% Ce added, evidencing that the selectivity to liquid phase products was undoubtedly favoured by doping with Ce.

Fig. 8 A displays the yield of the main liquid products obtained. For all the catalysts, 1,2-propanediol was the foremost product generated, which indicated that H_2 was indeed produced by APR. Hydroxyacetone, the major intermediate product in 1,2-propanediol formation, was the second leading liquid product. The high yields to both compounds, in addition to acetone (dehydration product of 1,2-propanediol), demonstrated high activity of the synthesized catalysts for the glycerol hydrodeoxygenation (HDO). Catalyst 0.3CeCoAl presented the maximum yield to 1,2-propanediol (34%) while 0CeCoAl and 2.1CeCoAl exhibited 28% and 25%, respectively. 0.3CeCoAl catalyst also manifested the highest yield to hydroxyacetone (22.6%). However, the utmost yield towards ethanol was achieved with pristine 0CeCoAl catalyst. The density and distribution of the acid sites is of important consideration in the production of by-products [65]. Ce-doped catalysts presented a higher density of medium and strong acid centers than pristine 0CeCoAl, which makes them better catalysts for dehydration reactions compared to bare cobalt aluminate catalyst that is conducive to dehydrogenation reactions.

Besides the liquid products displayed in Fig. 8A, 1-propanol was detected for all the catalysts. Concerning 0CeCoAl catalyst, a bunch of products was detected: propionic acid, acetic acid and very low amounts of 2-propanol, acetaldehyde and methanol. Obtaining this great variety of liquid products could be explained by the highest metal availability, and therefore a high reactivity, of the 0CeCoAl catalyst, which could facilitate the concatenation of successive dehydration/hydrogenation reactions. These results showed the relevance of the Ce-doped catalysts for 1,2-propanediol production from glycerol HDO with in-situ generated H_2. No liquids produced by Brønsted acid sites (acrolein, or 1,3-propanediol) were detected, indicating prevalence of the Lewis acidity.

Catalyst activity for bond cleavage was also analysed. From data in Fig. 8B it is shown that carbon selectivity to primary products (products from single C–C or C–O bond scission, such as ethylene glycol, hydroxyacetone and propylene glycol) was remarkable high for Ce-doped catalyst, 0.3CeCoAl and 2.1CeCoAl (82.5% and 79.6%, respectively). In turn, catalyst 0CeCoAl achieved 44.1% selectivity towards primary products while its selectivity to secondary ones (products obtained after cleavage of additional C-C or C-O bonds) was 24%, which is three-fold higher than that of Ce-doped catalysts. Pristine cobalt aluminate catalyst also attained a considerable selectivity to gas products (24.6%) in accordance with its high metallic surface area. Among the Ce-doped samples, catalyst 2.1CeCoAl displayed slightly lower selectivity to primary and secondary products than catalyst with 0.3% of cerium.

A summary of the reaction products is shown for the third hour TOS (Table 6). Carbon selectivity to ethylene glycol (EG) was around 5% for both Ce-doped catalysts and 3.3% for pristine 0CeCoAl. Carbon selectivity to 1,2-propanediol (1,2-PD) step up in the following order: 0CeCoAl (28.9%) < 2.1CeCoAl (42.4) < 0.3CeCoAl (46.5). Ce-containing catalysts also presented a higher selectivity towards hydroxyacetone (HA) (31–32%) compared to 0CeCoAl (11.9%). According to these results, Ce-doped catalysts can balance between acid centers (necessary for obtaining hydroxyacetone via glycerol dehydration) and metal availability for the further hydrogenation of hydroxyacetone into 1,2-propanediol. Both Ce-doped catalysts have less available Co^0, but of higher intrinsic activity as deduced from the cyclohexane dehydrogenation activities (Table 5). Ce-doped catalysts still have scope for improvement to decrease hydroxyacetone production in favour of 1,2-propanediol.

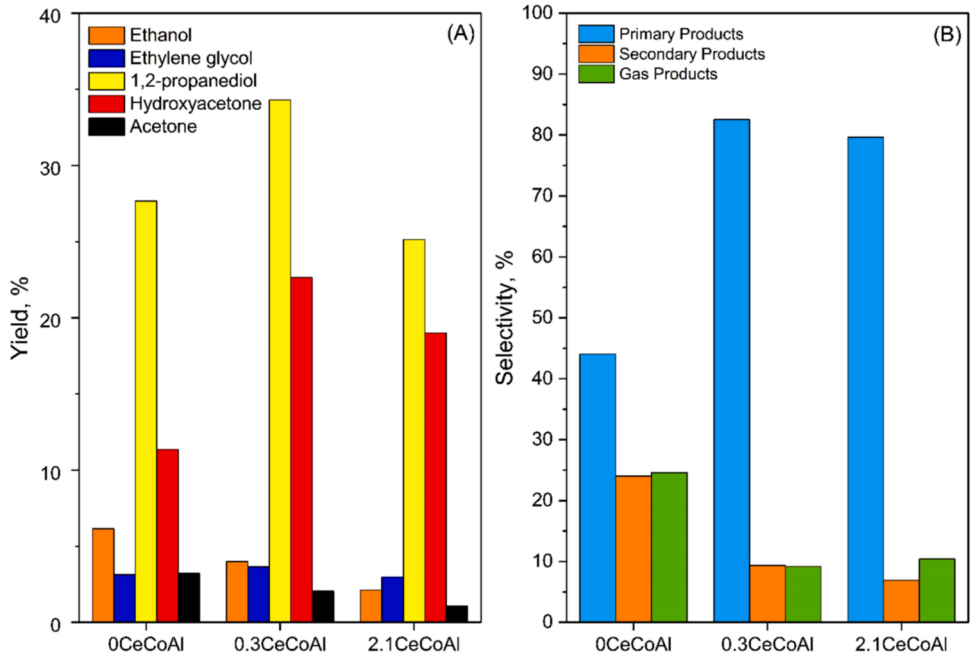

Fig. 8. (A) Liquids products distribution at 3 h TOS of glycerol APR at 260 °C/50 bar, and (B) Carbon selectivity by number of bond scissions. Primary Products: from single C–C or C–O bond scission; Secondary Products: from more than a single cleavages of C-C or C-O bonds; Gas products: C-containing gases.

Table 6
Liquid and gas products stream characteristics, at 3 h TOS, on glycerol HDO.

Catalysts	Carbon selectivity (%)			DOR[a] (%)	S_{C-C}[b]	S_{C-O}[b]	Y_{H2}[c] (%)	S_{alk}[d] (%)
	1,2-PD	HA	EG					
0CeCoAl	28.9	11.9	3.3	60.7	3.57	64.5	15.8	36.5
0.3CeCoAl	46.5	31.0	5.0	63.5	5.02	86.9	13.5	40.5
2.1CeCoAl	42.4	32.6	4.9	68.3	4.93	81.6	10.2	54.0

[a] degree of oxygen removal
[b] carbon selectivity by scission products in liquid phase
[c] hydrogen yield
[d] selectivity to alkanes

The low selectivity to hydroxyacetone and 1,2-propanediol presented by 0CeCoAl catalyst was due to the formation of other liquid compounds and its proficiency to break C-C bonds. In this sense, the formation of light alcohol and short chain alkanes is an inconvenience to be solved for the commercial development of this process for primary products [13].

The oxygen removal degree (DOR) reflects the ability of the catalysts to generate deoxygenated liquid compounds. Ce-doping enhanced DOR, as it passed from 60.7% for 0CeCoAl to 63.5–68.3% for 0.3 and 2.1CeCoAl. Liquid products were clustered into two main group. Products obtained by C–C bond cleavage only (ethylene glycol, methanol) and those classified as C–O bond scission products. The selectivity to both types of cleavage are given in Table 6. For all the catalysts, selectivity to C-O cleavage products (S_{C-O}) was considerable high (i.e. up to 86.9% for catalyst 0.3CeCoAl). In the same vein, 0CeCoAl catalyst presented the lowest value (S_{C-O} = 64.5%). In contrast, selectivity to S_{C-C} barely reached 5% (0.3CeCoAl). We can affirm that these catalysts, and particularly Ce-containing samples, exhibited excellent C–O bond scission function. Thus, the presence of cerium favoured the dehydration pathway, by slight increase of surface acid sites density, even under conditions in which cobalt aluminate based-catalysts have shown to favour dehydrogenation route [29].

Table 6 also gathered hydrogen yield (Y_{H2}) and selectivity to alkanes (S_{alk}). Regarding Y_{H2}, it follows the same trend as the liquid yield. It indicated that the obtained H_2 readily reacts to yield liquid products. Pristine 0CeCoAl showed the highest Y_{H2} and the lowest value was obtained for catalyst 2.1CeCoAl (10.2%). This catalyst, instead, displayed the maximum selectivity to alkanes (54%, mainly methane). In brief, selectivity towards alkanes increased with cerium content, which was evidenced by the decrease in Y_{H2}. It should be stressed that Y_{H2} reflects the hydrogen consumed in side reactions for the formation of both liquid and gaseous compounds while S_{alk} was calculated taking into account the flow of carbon atoms in alkanes with respect to the total carbon atoms only in gaseous products. These data lead us to conclude that, for catalyst 0CeCoAl, hydrogen produced in-situ is consumed mainly in the formation of diverse liquid products, while Ce-containing catalyst were more prone to the formation of alkanes.

3.8. Characterization of spent catalysts

A slight decrease in X_{Gly} and X_{liq} was observed in the course of reaction (Fig. S5, Supplementary Information), more pronounced for Ce-doped catalysts. From 2 h to 3 h TOS, X_{Gly} decreased by 9–14% for Ce-containing catalysts vs 2% for 0CeCoAl assay. In the same period, conversion to liquid decreased by 4–9% for the doped catalysts, while for the non-doped assay increased by 4%, which was due to the decrease in the production of gaseous compounds while the conversion of glycerol remains more stable. In order to investigate the potential changes in the physico-chemical properties underwent by catalysts in the reaction, the characterization of spent catalysts was carried out, and the results obtained are shown in Table 7.

N_2 adsorption-desorption isotherms and BJH pore size distribution of the spent catalysts are shown in Fig. 1. The form of the isotherms of the spent catalysts resembled those of fresh reduced solids, indicating the pore structure was preserved. All the spent catalysts adsorbed more nitrogen than the parent fresh reduced solid, which, in turn, was reflected in the increase in S_{BET}. Spent 0CeCoAl catalysts showed 75% increment in S_{BET}, while Ce-doped catalysts incremented by 26–57%. Reynoso el at. observed that hydrated alumina species were involved in the specific surface area gain [29]. Under hydrothermal conditions γ-alumina could be hydrated to gibbsite or boehmite, which in turn,

Tablee 7
Textural properties and leaching concentration of xCeCoAl used samples.

Catalyst	S_{BET} (m^2/g)	V_{pore} (cm^3/g)	d_{pore} (nm)	Metals leached (wt %)			H_2 uptake up to 600 °C ($mmol_{H2}$/g)	Exposed Co° sites[a] (at.$_{Co°}$/g)	$C_{deposits}$ (μmol_C/g_{cat})
				Al	Co	Ce			
0CeCoAl	178.2 (+75%)	0.411 (+10%)	8.0 (−17%)	1.5	1.6	–	2.30	$9.92{\cdot}10^{17}$ (−96%)	0.72
0.3CeCoAl	174.4 (+26%)	0.414 (+3%)	7.8 (−10%)	2.1	3.5	0.12	2.06	$4.10{\cdot}10^{18}$ (−72%)	0.44
2.1CeCoAl	206.7 (+57%)	0.598 (+41%)	9.3 (−4%)	2.3	4.8	0.63	1.40	$4.68{\cdot}10^{18}$ (−64%)	0.17

In parenthesis, percentage variation respect freshly reduced forms.
[a] from H_2 chemisorption. Values in parenthesis, percentage variation respect freshly reduced forms

could be leached-off and re-deposited on the catalyst surface, generating additional porosity in the solid [66]. Differences between reduced and spent catalysts were appreciated in the BJH pore size distribution. Spent catalysts had bimodal distributions, with maxima at approximately 3–4 nm and 8–10 nm pores. The peak from smaller pores suggested the presence of new phases not observed in the fresh reduced form (e.g. gibbsite or cerium hydroxycarbonate). The former narrow peak was more pronounced for solids with higher amount of cerium. Many phenomena could explain this evolution of the textural properties, such as hydration of the alumina [67], deposits of carbonaceous materials [68] or the formation of new phases [69].

Crystalline phases in the exhausted catalysts were identified by XRD (Fig. 9A). The obtained diffractograms still showed the well-known characteristic peaks of spinel (either cobalt oxide and cobalt aluminate). XRD reflexions from metallic Co were still visible for all catalysts. The poor resolution of the spectra from those peaks prevented us to calculate the crystallite size. We could hypothesize that coalescense of metallic cobalt was not significant, despite of the high temperature used. A new peak at around 34° (2θ) emerged for all spent catalysts, which corresponded to cubic CoO phase (PDF 048-1719). This fact indicated that cobalt could be oxidized in the aqueous media of the reaction [70, 71]. It could be concluded that the oxidation of cobalt was limited to the outmost caps of the particles, since XRD signal from bulk Co^0 remained. None of the spent catalysts showed diffraction peaks from hydrated alumina (boehmite or gibbsite), which could be due to its amorphous form. For Ce-doped catalysts, new XRD peaks arose and became significant for 2.1CeCoAl catalyst. Those peaks centred at 24.6° and 30.6° were attributable to the hexagonal phase of cerium hydroxycarbonate ($Ce(CO_3)OH$) (PDF 32-0189). This new phase was formed by carbonation of ceria by the CO formed, promoted by the harsh hydrothermal conditions [72]. Cerium hydroxycarbonate has been also detected in the spent Ni/CeO_2 catalysts after usage in the aqueous-phase reforming of methanol [73]. The sharpness of these Ce-containing new phase peaks indicated that the product was well crystallized. All the Ce-containing spent catalysts showed peaks from Ce_5Co_{19} phase structure, though weakened with respect the reduced form.

Leaching of catalyst components contribute to the deactivation of heterogeneous catalysts in the liquid-phase reactions [22]. Accordingly, the catalysts metal constituents Al, Ce and Co in the reaction liquid product were analysed by ICP-MS. All spent catalysts experienced leaching of the three metals, to a different extent. At first glance, Ce-containing catalysts underwent greater leaching of all metals. Cobalt was the most leached metal and the percentage of leaching in the Ce-containing samples was 2–3 times higher than for catalysts 0CeCoAl. This behaviour could be due to the smaller size of metallic Co in the Ce-doped catalysts, which are more prone to oxidation and subsequent leaching [74]. Co was thermodynamically prone to be oxidized (preliminary stage of leaching), also the phase transition during alumina hydration could promote metal particle detachment. Due to the re-deposition of aluminium hydroxyde on the catalyst surface, leaching

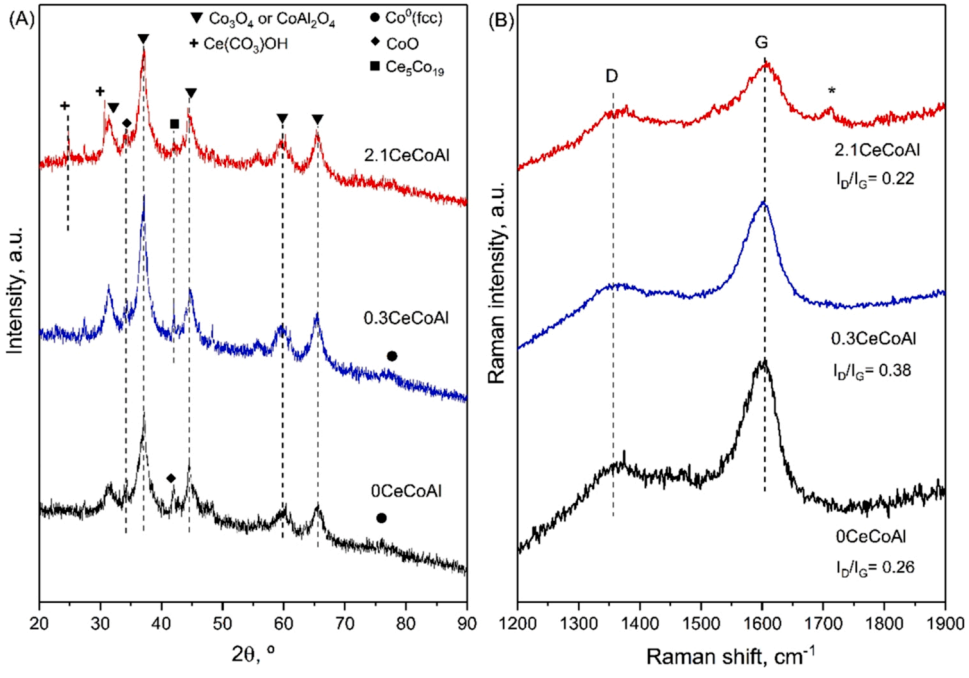

Fig. 9. (A) XRD patterns and (B) Raman spectra of the spent xCeCoAl catalysts.

of aluminium was 1–2 less intense than cobalt. Meanwhile, the amount of Ce leached out from the catalysts increased in proportion to the amount of Ce in the samples.

The spent catalysts were also subjected to H_2-TPR analysis (Fig. S56, Supplementary Information) and the hydrogen uptake values are reported in Table 7. The hydrogen consumption was higher than the required for the reduction of solely cobalt species (deduced through the reducibility degree). Indeed, all samples showed hydrogen consumption below 600 °C, which indicated the catalysts were oxidized in the course of the reaction. It is also noteworthy the intense H_2 consumption at temperatures above 600 °C. Actually, the used catalysts showed negligible consumption below 500 °C. Other authors [75] have investigated reduction temperature range after and before reactions, concluding that spent catalysts show a shift towards higher temperatures compared to fresh one due to the aggregation or sintering of metal clusters.

Overall, the metallic availability of all catalysts was seriously compromised, as was also confirmed by H_2 chemisorption that revealed a decrease of about 64% for catalyst 2.1CeCoAl and up to 96% for monometallic 0CeCoAl. One plausible explanation is the re-deposition of aluminium on the catalyst surface, covering the Co^0 sites by hydrated alumina [76,77]. Two other phenomena that cannot be ignored are the oxidation of cobalt and the preferential leaching of the smallest particles, thus remaining the largest particles, consequently reducing accessible metal atoms [78,79].

The results obtained by TPH, displayed in Table 7, present a very low deposition of carbonaceous material, which decreased with the Ce-content. The recorded Raman spectra of the used catalysts (Fig. 9B) exhibited the typical peaks from carbon, named D and G bands, at ca. 1350 and 1590–1600 cm^{-1}, respectively. The shape of the spectra was similar for all catalysts with a broad and less intense D-band and a more intense G-band. The shoulder observed at 1710 cm^{-1} in the sample 2.1CeCoAl could be attributed to an overtone of an M point phonon [80]. The degree of graphitization of carbonaceous materials was estimated by the relative intensity ratio of D and G bands (I_D/I_G inset in Fig. 9B). The I_D/I_G values obtained were in the 0.22–0.38 range and did not show correlation with the composition of the samples. Raman and TPH agree with the absence of any peak from coke in the XRD pattern. It seems that the principal deactivation issues are those related to the loss of metal surface area, due to the encapsulation by alumina, and the oxidation of cobalt species. Cobalt oxidation could lead to metal leaching, another phenomenon responsible for the decrease in the metal surface.

4. Conclusions

The effect of Ce-coprecipitation to improve the activity and selectivity of cobalt aluminate-based catalysts for glycerol HDO was discussed. Properties of catalysts based on cobalt aluminate spinels were tuned through Ce doping, a simple, fast and cost-effective synthesis method. Ce-modification of the 0CeCoAl catalyst increased S_{BET} (by around 16–30%) and also the spinel crystallite size. For the reduced sample, in addition to cobalt aluminate and metallic cobalt species, formation of Ce_5Co_{19} phase was identified at the highest Ce-content. Also, Ce-doping increased total acidity through a prominent increment of medium-strong acid centers.

Ce-doped catalysts exhibited lower glycerol conversion than their counterpart, 0CeCoAl. Nevertheless, their higher acid sites density have influenced the activity of these catalysts, presenting a higher selectivity towards deoxygenated liquid products. Catalyst testing in a fixed-bed reactor at 260 °C and 50 bar without external hydrogen source revealed that: (i) H_2 is produced; and (ii) it is in part consumed hydrogenating liquid intermediates, which makes these catalysts to have advantageous catalytic properties for glycerol HDO in a sustainable way. The main products of glycerol conversion were 1,2-propanediol and hydroxyacetone. Selectivity to liquid products of catalyst 0.3CeCoAl was 92% and selectivity to 1,2-propanediol was over 46%, indicating that Ce-doped catalysts are compelling HDO catalysts.

Future research should focus on stability issues since post-reaction characterization verified a decrease in cobalt availability that can be attributed to re-deposition of hydrated alumina on the catalyst surface. This phenomenon, in conjunction with the deposition of carbonaceous material, could be responsible for the increment in S_{BET} and the change in the pore size distribution. Further confirmed fact was that despite the addition of cerium, the catalysts continued to exhibit metal oxidation and leaching phenomena.

CRediT authorship contribution statement

A.J. Reynoso: Investigation, Writing – original draft. **U. Iriarte-Velasco**: Formal analysis, Writing – review & editing. **M.A. Gutiérrez-Ortiz**: Resources, Funding acquisition, Supervision. **J.L. Ayastuy**: Funding acquisition, Conceptualization, Writing – review & editing.

Declaration of Competing Interest

The authors declare that they have no known competing financial interests or personal relationships that could have appeared to influence the work reported in this paper.

Acknowledgements

This research was supported by grant PID2019-106692EB-I00 funded by MCIN/AEI/10.13039/501100011033. The authors thank for technical support provided by SGIker of UPV/EHU and European funding (ERDF and ESF). Cyclohexane dehydrogenation and isomerization of 33DM1B model reaction were conducted at the Institut de Chimie des Milieux et des Matériaux, Université de Poitiers, (CNRS UMR 7285 IC2MP). The authors acknowledge the kind assistance of Dr. Catherine Especel and Dr. Laurence Vivier.

Appendix A. Supporting information

Supplementary data associated with this article can be found in the online version at doi:10.1016/j.jece.2022.107612.

References

[1] J. Spekreijse, T. Lammens, C. Parisi, T. Ronzon, M. Vis, Insights into the European Market for Bio-based Chemicals, EUR 29581 EN, Publications Office of the European Union, Luxembourg, 2019, JRC112989, https://doi.org/10.2760/739561.
[2] K. Kohli, R. Prajapati, B.K. Sharma, Bio-based chemicals from renewable biomass for integrated biorefineries, Energies 12 (2) (2019) 233, https://doi.org/10.3390/en12020233.
[3] F. Cherubini, The biorefinery concept: using biomass instead of oil for producing energy and chemicals, Energy Convers. Manag. 51 (2010) 1412–1421, https://doi.org/10.1016/j.enconman.2010.01.015.
[4] J.J. Bozell, G.R. Petersen, Technology development for the production of biobased products from biorefinery carbohydrates—the US Department of Energy's "Top 10" revisited, Green Chem. 12 (2010) 539–554.
[5] I.C. Freitas, R.L. Manfro, M.M.V.M. Souza, Hydrogenolysis of glycerol to propylene glycol in continuous system without hydrogen addition over Cu-Ni catalysts, Appl. Catal. B Environ. 220 (2018) 31–41, https://doi.org/10.1016/j.apcatb.2017.08.030.
[6] B.C.M. Morales, B.A.O. Quesada, Conversion of glycerol to hydroxyacetone over Cu and Ni catalysts, Catal. Today 372 (2021) 115–125, https://doi.org/10.1016/j.cattod.2020.11.025.
[7] A. Talebian-Kiakalaieh, N.A.S. Amin, H. Hezaveh, Glycerol for renewable acrolein production by catalytic dehydration, Renew. Sustain. Energy Rev. 40 (2014) 28–59, https://doi.org/10.1016/j.rser.2014.07.168.
[8] B. Katryniok, H. Kimura, E. Skrzyńska, J. Girardon, P. Fongarland, M. Capron, R. Ducoulombier, N. Mimura, S. Paul, F. Dumeignil, Selective catalytic oxidation of glycerol: perspectives for high value chemicals, Green Chem. 13 (2011) 1960–1979, https://doi.org/10.1039/C1GC15320J.
[9] Y. Li, M. Nielsen, B. Li, P.H. Dixneuf, H. Junge, M. Beller, Ruthenium-catalyzed hydrogen generation from glycerol and selective synthesis of lactic acid, Green Chem. 17 (2015) 193–198, https://doi.org/10.1039/C4GC01707B.
[10] R.K.P. Purushothaman, J. van Haveren, A. Mayoral, I. Melián-Cabrera, H.J. Heeres, Exploratory catalyst screening studies on the base free conversion of glycerol to

lactic acid and glyceric acid in water using bimetallic Au–Pt nanoparticles on acidic zeolites, Top. Catal. 57 (2014) 1445–1453, https://doi.org/10.1007/s11244-014-0316-2.
[11] Y. Nakagawa, K. Tomishige, Heterogeneous catalysis of the glycerol hydrogenolysis, Catal. Sci. Technol. 1 (2011) 179–190, https://doi.org/10.1039/C0CY00054J.
[12] C.J. Sullivan, A. Kuenz, K. Vorlop, Propanediols, Ullmann's Encyclopedia of Industrial Chemistry, (2018), 1–15.
[13] Y. Liu, C.T.Q. Mai, F.T.T. Ng, Glycerol hydrogenolysis with in situ hydrogen produced via methanol steam reforming: the promoting effect of Pd on a Cu/ZnO/Al_2O_3 catalyst, Catalysts 11 (1) (2021) 110, https://doi.org/10.3390/catal11010110.
[14] S.N. Delgado, D. Yap, L. Vivier, C. Especel, Influence of the nature of the support on the catalytic properties of Pt-based catalysts for hydrogenolysis of glycerol, J. Mol. Catal. A Chem. 367 (2013) 89–98, https://doi.org/10.1016/j.molcata.2012.11.001.
[15] V. Yfanti, D. Ipsakis, A.A. Lemonidou, Kinetic study of liquid phase glycerol hydrodeoxygenation under inert conditions over a Cu-based catalyst, React. Chem. Eng. 3 (2018) 559–571, https://doi.org/10.1039/C8RE00061A.
[16] M.A. Dasari, P. Kiatsimkul, W.R. Sutterlin, G.J. Suppes, Low-pressure hydrogenolysis of glycerol to propylene glycol, Appl. Catal. A Gen. 281 (2005) 225–231, https://doi.org/10.1016/j.apcata.2004.11.033.
[17] P. Kumar, A.K. Shah, J. Lee, Y.H. Park, U.L. Štangar, Selective hydrogenolysis of glycerol over bifunctional copper–magnesium-supported catalysts for propanediol synthesis, Ind. Eng. Chem. Res. 59 (2020) 6506–6516, https://doi.org/10.1021/acs.iecr.9b06978.
[18] H. Gong, X. Zhao, X. Li, M. Chen, Y. Ma, J. Fang, X. Wei, Q. Peng, Z. Hou, Boosting the long-term stability of hydrotalcite-derived catalysts in hydrogenolysis of glycerol by incorporation of Ca(II), ACS Sustain. Chem. Eng. 9 (2021) 2246–2259, https://doi.org/10.1021/acssuschemeng.0c08033.
[19] X. Guo, Y. Li, R. Shi, Q. Liu, E. Zhan, W. Shen, Co/MgO catalysts for hydrogenolysis of glycerol to 1, 2-propanediol, Appl. Catal. A Gen. 371 (2009) 108–113, https://doi.org/10.1016/j.apcata.2009.09.037.
[20] V. Rekha, C. Sumana, S.P. Douglas, N. Lingaiah, Understanding the role of Co in Co–ZnO mixed oxide catalysts for the selective hydrogenolysis of glycerol, Appl. Catal. A Gen. 491 (2015) 155–162, https://doi.org/10.1016/j.apcata.2014.10.042.
[21] T.K. Phung, T.L.M. Pham, A.T. Nguyen, K.B. Vu, H.N. Giang, T. Nguyen, T. C. Huynh, H.D. Pham, Effect of supports and promoters on the performance of Ni-based catalysts in ethanol steam reforming, Chem. Eng. Technol. 43 (2020) 672–688, https://doi.org/10.1002/ceat.201900445.
[22] I. Sádaba, M. López Granados, A. Riisager, E. Taarning, Deactivation of solid catalysts in liquid media: the case of leaching of active sites in biomass conversion reactions, Green Chem. 17 (2015) 4133–4145, https://doi.org/10.1039/C5GC00804B.
[23] I. Coronado, M. Pitínová, R. Karinen, M. Reinikainen, R.L. Puurunen, J. Lehtonen, Aqueous-phase reforming of Fischer-Tropsch alcohols over nickel-based catalysts to produce hydrogen: product distribution and reaction pathways, Appl. Catal. A Gen. 567 (2018) 112–121, https://doi.org/10.1016/j.apcata.2018.09.013.
[24] R.L. Manfro, A.F. Da Costa, N.F.P. Ribeiro, M.M.V.M. Souza, Hydrogen production by aqueous-phase reforming of glycerol over nickel catalysts supported on CeO_2, Fuel Process. Technol. 92 (2011) 330–335, https://doi.org/10.1016/j.fuproc.2010.09.024.
[25] M.L. Barbelli, F. Pompeo, G.F. Santori, N.N. Nichio, Pt catalyst supported on α-Al_2O_3 modified with CeO_2 and ZrO_2 for aqueous-phase-reforming of glycerol, Catal. Today 213 (2013) 58–64, https://doi.org/10.1016/j.cattod.2013.02.023.
[26] M.M. Rahman, T.L. Church, A.I. Minett, A.T. Harris, Effect of CeO_2 addition to Al_2O_3 supports for Pt catalysts on the aqueous-phase reforming of glycerol, ChemSusChem 6 (2013) 1006–1013, https://doi.org/10.1002/cssc.201200797.
[27] A. Chen, H. Guo, Y. Song, P. Chen, H. Lou, Recyclable CeO_2–ZrO_2 and CeO_2–TiO_2 mixed oxides based Pt catalyst for aqueous-phase reforming of the low-boiling fraction of bio-oil, Int. J. Hydrog. Energy 42 (2017) 9577–9588, https://doi.org/10.1016/j.ijhydene.2017.03.092.
[28] B. Roy, C.A. Leclerc, Study of preparation method and oxidization/reduction effect on the performance of nickel-cerium oxide catalysts for aqueous-phase reforming of ethanol, J. Power Sources 299 (2015) 114–124, https://doi.org/10.1016/j.jpowsour.2015.08.069.
[29] A.J. Reynoso, J.L. Ayastuy, U. Iriarte-Velasco, M.A. Gutiérrez-Ortiz, Cobalt aluminate spinel-derived catalysts for glycerol aqueous phase reforming, Appl. Catal. B Environ. 239 (2018) 86–101, https://doi.org/10.1016/j.apcatb.2018.08.001.
[30] R.C. Reuel, C.H. Bartholomew, The stoichiometries of H_2 and CO adsorptions on cobalt: Effects of support and preparation, J. Catal. 85 (1984) 63–77, https://doi.org/10.1016/0021-9517(84)90110-6.
[31] B. Jongsomjit, J.G. Goodwin, Co-support compound formation in Co/Al_2O_3 catalysts: effect of reduction gas containing CO, Catal. Today 77 (3) (2002) 191–204, https://doi.org/10.1016/S0920-5861(02)00245-6.
[32] N. Hérault, L. Olivet, L. Pirault-Roy, C. Especel, M.A. Vicerich, C.L. Pieck, F. Epron, Controlled preparation and characterization of Pt-Rh/Al_2O_3 bimetallic catalysts for reactions in reducing conditions, Appl. Catal. A Gen. 517 (2016) 81–90, https://doi.org/10.1016/j.apcata.2016.02.024.
[33] S.A. D'Ippolito, L. Pirault-Roy, C. Especel, F. Epron, C.L. Pieck, Influence of rhodium content on the behavior of Rh/SiO_2–Al_2O_3 catalysts for selective ring opening of decalin, RSC Adv. 7 (2017) 46803–46811, https://doi.org/10.1039/C7RA08350E.
[34] P. Sahoo, H. Djieutedjeu, P.F.P. Poudeu, Co_3O_4 nanostructures: the effect of synthesis conditions on particles size, magnetism and transport properties, J. Mater. Chem. A 1 (2013) 15022–15030, https://doi.org/10.1039/C3TA13442C.
[35] N. Ouahdi, S. Guillemet, B. Durand, R.E. Ouatib, L.E. Rakho, R. Moussa, A. Samdi, Synthesis of $CoAl_2O_4$ by double decomposition reaction between $LiAlO_2$ and molten $KCoCl_3$, J. Eur. Ceram. Soc. 28 (2008) 1987–1994, https://doi.org/10.1016/j.jeurceramsoc.2007.12.035.
[36] P. Li, X. Chen, L. Ma, A. Bhat, Y. Li, J.W. Schwank, Effect of Ce and La dopants in Co_3O_4 nanorods on the catalytic activity of CO and C_3H_6 oxidation, Catal. Sci. Technol. 9 (2019) 1165–1177, https://doi.org/10.1039/C8CY02460J.
[37] F. Ali, N.R. Khalid, G. Nabi, A. Ul-Hamid, M. Ikram, Hydrothermal synthesis of cerium-doped Co_3O_4 nanoflakes as electrode for supercapacitor application, Int. J. Energy Res. 45 (2021) 1999–2010, https://doi.org/10.1002/er.5893.
[38] O.M. Hemeda, M.A. Amer, S. Aboul-Enein, M.A. Ahmed, Effect of sintering on X-Ray and IR spectral behaviour of the $MnAl_xFe_{2-x}O_4$ ferrite system, Phys. Stat. Sol. (A) 156 (1996) 29–38, https://doi.org/10.5185/amlett.2012.10431.
[39] K. Karásková, K. Pacultová, A. Klegova, D. Fridrichová, M. Valášková, K. Jirátová, P. Stelmachowski, A. Kotarba, L. Obalová, Magnesium effect in K/Co-Mg-Mn-Al mixed oxide catalyst for direct NO decomposition, Catalysts 10 (8) (2020) 931, https://doi.org/10.3390/catal10080931.
[40] N. Srisawad, W. Chaitree, O. Mekasuwandumrong, P. Praserthdam, J. Panpranot, Formation of $CoAl_2O_4$ nanoparticles via low-temperature solid-state reaction of fine gibbsite and cobalt precursor, J. Nanomater. (2012) (2012), 108369, https://doi.org/10.1155/2012/108369.
[41] Z. Zsoldos, L. Guczi, Structure and catalytic activity of alumina supported platinum-cobalt bimetallic catalysts. 3. Effect of treatment on the interface layer, J. Phys. Chem. 96 (1992) 9393–9400, https://doi.org/10.1021/j100202a061.
[42] X. Duan, M. Pan, F. Yu, D. Yuan, Synthesis, structure and optical properties of $CoAl_2O_4$ spinel nanocrystals, J. Alloy. Compd. 509 (2011) 1079–1083, https://doi.org/10.1016/j.jallcom.2010.09.199.
[43] E. Bèche, P. Charvin, D. Perarnau, S. Abanades, G. Flamant, Ce 3d XPS investigation of cerium oxides and mixed cerium oxide ($Ce_xTi_yO_z$), Surf. Interface Anal. 40 (2008) 264–267, https://doi.org/10.1002/sia.2686.
[44] Y. Kuo, C. Lee, Y. Chen, H. Liang, Gadolinia-doped ceria films deposited by RF reactive magnetron sputtering, Solid State Ion. 180 (2009) 1421–1428, https://doi.org/10.1016/j.ssi.2009.08.016.
[45] Y.A. Teterin, A.Y. Teterin, A.M. Lebedev, I.O. Utkin, The XPS spectra of cerium compounds containing oxygen, J. Electron Spectrosc. Relat. Phenom. 88–91 (1998) 275–279, https://doi.org/10.1016/S0368-2048(97)00139-4.
[46] Y. Liu, H. Dai, J. Deng, S. Xie, H. Yang, W. Tan, W. Han, Y. Jiang, G. Guo, Mesoporous Co_3O_4-supported gold nanocatalysts: highly active for the oxidation of carbon monoxide, benzene, toluene, and o-xylene, J. Catal. 309 (2014) 408–418, https://doi.org/10.1016/j.jcat.2013.10.019.
[47] M. Sun, W. Li, B. Zhang, G. Cheng, B. Lan, F. Ye, Y. Zheng, X. Cheng, L. Yu, Enhanced catalytic performance by oxygen vacancy and active interface originated from facile reduction of OMS-2, Chem. Eng. J. 331 (2018) 626–635, https://doi.org/10.1016/j.cej.2017.09.028.
[48] M. Kong, Y. Li, X. Chen, T. Tian, P. Fang, F. Zheng, X. Zhao, Tuning the relative concentration ratio of bulk defects to surface defects in TiO_2 nanocrystals leads to high photocatalytic efficiency, J. Am. Chem. Soc. 133 (2011) 16414–16417, https://doi.org/10.1021/ja207826q.
[49] S. Kannan, C.S. Swamy, Catalytic decomposition of nitrous oxide over calcined cobalt aluminum hydrotalcites, Catal. Today 53 (1999) 725–737, https://doi.org/10.1016/S0920-5861(99)00159-5.
[50] G. Ranga Rao, H.R. Sahu, XRD and UV-Vis diffuse reflectance analysis of CeO_2-ZrO_2 solid solutions synthesized by combustion method, J. Chem. Sci. 113 (2001) 651–658, https://doi.org/10.1007/BF02708797.
[51] J. Vakros, C. Kordulis, A. Lycourghiotis, Cobalt oxide supported γ-alumina catalyst with very high active surface area prepared by equilibrium deposition filtration, Langmuir 18 (2002) 417–422, https://doi.org/10.1021/la010040w.
[52] A.A. Verberckmoes, B.M. Weckhuysen, R.A. Schoonheydt, Spectroscopy and coordination chemistry of cobalt in molecular, Microporous Mesoporous Mater. 22 (1998) 165–178, https://doi.org/10.1016/S1387-1811(98)00091-2.
[53] A. Getsoian, Z. Zhai, A.T. Bell, Band-gap energy as a descriptor of catalytic activity for propene oxidation over mixed metal oxide catalysts, J. Am. Chem. Soc. 136 (2014) 13684–13697, https://doi.org/10.1021/ja5051555.
[54] E. Regulska, J. Breczko, A. Basa, A.T. Dubis, Rare-earth metals-doped nickel aluminate spinels for photocatalytic degradation of organic pollutants, Catalysts 10 (9) (2020) 1003, https://doi.org/10.3390/catal10091003.
[55] N. Zhang, Q. Qin, X. Ma, J. Zhou, L. Sun, C. Chen, S. Wen, Y. Chen, S. Ruan, One-step synthesis and gas sensing properties of hierarchical Fe doped Co_3O_4 nanostructures, J. Alloy. Compd. 723 (2017) 779–786, https://doi.org/10.1016/j.jallcom.2017.06.301.
[56] S. Xu, N.R. Jaegers, W. Hu, J.H. Kwak, X. Bao, J. Sun, Y. Wang, J.Z. Hu, High-field one-dimensional and two-dimensional ^{27}Al magic-angle spinning nuclear magnetic resonance study of θ-, δ-, and γ-Al_2O_3 dominated aluminum oxides: toward understanding the Al sites in γ-Al_2O_3, ACS Omega 6 (5) (2021) 4090–4099, https://doi.org/10.1021/acsomega.0c06163.
[57] L.A. O'Dell, S.L.P. Savin, A.V. Chadwick, M.E. Smith, A ^{27}Al MAS NMR study of a sol–gel produced alumina: Identification of the NMR parameters of the θ-Al_2O_3 transition alumina phase, Solid State Nucl. Magn. Reson. 31 (2007) 169–173, https://doi.org/10.1016/j.ssnmr.2007.05.002.
[58] Y. Zheng, Y. Yu, H. Zhou, W. Huang, Z. Pu, Combustion of lean methane over Co_3O_4 catalysts prepared with different cobalt precursors, RSC Adv. 10 (2020) 4490–4498, https://doi.org/10.1039/C9RA09544F.

[59] J.L. Ayastuy, A. Gurbani, M.P. González-Marcos, M.A. Gutiérrez-Ortiz, Selective CO oxidation in H_2 streams on $CuO/Ce_xZr_{1-x}O_2$ catalysts: correlation between activity and low temperature reducibility, Int. J. Hydrog. Energy 37 (2012) 1993–2006, https://doi.org/10.1016/j.ijhydene.2011.04.178.
[60] H.H. Kung, Catalytic behavior of a cation in a solid solution—an electrostatic potential approach, J. Catal. 73 (1982) 387–395, https://doi.org/10.1016/0021-9517(82)90111-7.
[61] B. Jongsomjit, J. Panpranot, J.G. Goodwin Jr., Co-support compound formation in alumina-supported cobalt catalysts, J. Catal. 204 (2001) 98–109, https://doi.org/10.1006/jcat.2001.3387.
[62] C. Morterra, G. Magnacca, Surface characterization of modified aluminas. Part 5.—Surface acidity and basicity of CeO_2–Al_2O_3 systems, J. Chem. Soc. Faraday Trans. 92 (1996) 5111–5116, https://doi.org/10.1039/FT9969205111.
[63] B. Hu, W. Kim, T.P. Sulmonetti, M.L. Sarazen, S. Tan, J. So, Y. Liu, R.S. Dixit, S. Nair, C.W. Jones, A mesoporous cobalt aluminate spinel catalyst for nonoxidative propane dehydrogenation, ChemCatChem 9 (2017) 3330–3337, https://doi.org/10.1002/cctc.201700647.
[64] Y.T. Kim, K. Jung, E.D. Park, Gas-phase dehydration of glycerol over silica–alumina catalysts, Appl. Catal. B Environ. 107 (2011) 177–187, https://doi.org/10.1016/j.apcatb.2011.07.011.
[65] M.N. Gatti, J.L. Cerioni, F. Pompeo, G.F. Santori, N.N. Nichio, High yield to 1-Propanol from crude glycerol using two reaction steps with Ni catalysts, Catalysts 10 (6) (2020) 615, https://doi.org/10.3390/catal10060615.
[66] R.M. Ravenelle, J.R. Copeland, W. Kim, J.C. Crittenden, C. Sievers, Structural changes of γ-Al_2O_3-supported catalysts in hot liquid water, ACS Catal. 1 (2011) 552–561, https://doi.org/10.1021/cs1001515.
[67] N.H. Tran, G.S.K. Kannangara, Conversion of glycerol to hydrogen rich gas, Chem. Soc. Rev. 42 (2013) 9454–9479, https://doi.org/10.1039/C3CS60227C.
[68] I. Pala-Rosas, J.L. Contreras, J. Salmones, B. Zeifert, R. López-Medina, J. Navarrete-Bolaños, S. Hernández-Ramírez, J. Pérez-Cabrera, A.A. Fragoso-Montes de Oca, Catalytic deactivation of HY zeolites in the dehydration of glycerol to acrolein, Catalysts 11 (3) (2021) 360, https://doi.org/10.3390/catal11030360.
[69] R.M. Ravenelle, F. Schüβler, A. D'Amico, N. Danilina, J.A. van Bokhoven, J. A. Lercher, C.W. Jones, C. Sievers, Stability of zeolites in hot liquid water, J. Phys. Chem. C 114 (2010) 19582–19595, https://doi.org/10.1021/jp104639e.
[70] C. Sievers, Y. Noda, L. Qi, E.M. Albuquerque, R.M. Rioux, S.L. Scott, Phenomena affecting catalytic reactions at solid–liquid interfaces, ACS Catal. 6 (2016) 8286–8307, https://doi.org/10.1021/acscatal.6b02532.
[71] E. van Steen, M. Claeys, M.E. Dry, J. van de Loosdrecht, E.L. Viljoen, J.L. Visagie, Stability of nanocrystals: thermodynamic analysis of oxidation and re-reduction of cobalt in water/hydrogen mixtures, J. Phys. Chem. B 109 (2005) 3575–3577, https://doi.org/10.1021/jp045136o.
[72] Y. He, X. Liang, B. Chen, Globin-like mesoporous CeO_2: A CO-assisted synthesis based on carbonate hydroxide precursors and its applications in low temperature CO oxidation, Nano Res. 8 (2015) 1269–1278, https://doi.org/10.1007/s12274-014-0614-9.
[73] M. Stekrova, A. Rinta-Paavola, R. Karinen, Hydrogen production via aqueous-phase reforming of methanol over nickel modified Ce, Zr and La oxide supports, Catal. Today 304 (2018) 143–152, https://doi.org/10.1016/j.cattod.2017.08.030.
[74] T. van Haasterecht, M. Swart, K.P. de Jong, J.H. Bitter, Effect of initial nickel particle size on stability of nickel catalysts for aqueous phase reforming, J. Energy Chem. 25 (2016) 289–296, https://doi.org/10.1016/j.jechem.2016.01.006.
[75] J. Beckers, G. Rothenberg, Redox properties of doped and supported copper–ceria catalysts, Dalton Trans. (2008) 6573–6578, https://doi.org/10.1039/B809769K.
[76] J. Tao, L. Hou, B. Yan, G. Chen, W. Li, H. Chen, Z. Cheng, F. Lin, Hydrogen production via aqueous-phase reforming of ethylene glycol over a nickel–iron alloy catalyst: effect of cobalt addition, Energy Fuels 34 (2) (2020) 1153–1161, https://doi.org/10.1021/acs.energyfuels.9b02149.
[77] D.J.M. de Vlieger, L. Lefferts, K. Seshan, Ru decorated carbon nanotubes – a promising catalyst for reforming bio-based acetic acid in the aqueous phase, Green Chem. 16 (2014) 864–874, https://doi.org/10.1039/C3GC41922C.
[78] C.H. Zhou, K. Deng, M.D. Serio, S. Xiao, D.S. Tong, L. Li, C.X. Lin, J. Beltramini, H. Zhang, W.H. Yua, Cleaner hydrothermal hydrogenolysis of glycerol to 1,2-propanediol over Cu/oxide catalysts without addition of external hydrogen, Mol. Catal. 432 (2017) 274–284, https://doi.org/10.1016/j.mcat.2017.02.008.
[79] F. Cai, D. Pan, J.J. Ibrahim, J. Zhang, G. Xiao, Hydrogenolysis of glycerol over supported bimetallic Ni/Cu catalysts with and without external hydrogen addition in a fixed-bed flow reactor, Appl. Catal. A Gen. 564 (2018) 172–182, https://doi.org/10.1016/j.apcata.2018.07.029.
[80] J.C. Burton, L. Sun, F.H. Long, Z.C. Feng, I.T. Ferguson, First- and second-order Raman scattering from semi-insulating 4H–SiC, Phys. Rev. B 59 (1999) 7282–7284, https://doi.org/10.1103/PhysRevB.59.7282.